No detectable influence of the carbonate ion effect on changes in stable carbon isotope ratios (δ^{13}C) of shallow dwelling planktic foraminifera over the past 160 kyr

Peter Köhler[1] **and Stefan Mulitza**[2]

[1]Alfred-Wegener-Institut Helmholtz-Zentrum für Polar- und Meeresforschung, Bremerhaven, Germany
[2]MARUM – Center for Marine Environmental Sciences and Faculty of Geosciences,
University of Bremen, Bremen, Germany

Correspondence: Peter Köhler (peter.koehler@awi.de)

Abstract. Laboratory experiments showed that the isotopic fractionation of δ^{13}C and of δ^{18}O during calcite formation of planktic foraminifera are species-specific functions of ambient CO_3^{2-} concentration. This effect became known as the carbonate ion effect (CIE), whose role for the interpretation of marine sediment data will be investigated here in an in-depth analysis of the ^{13}C cycle. For this investigation, we constructed new 160 kyr long mono-specific stacks of changes in both δ^{13}C and δ^{18}O from either the planktic foraminifera *Globigerinoides ruber* (rub) or *Trilobatus sacculifer* (sac) from 112 and 40 marine records, respectively, from the wider tropics (latitudes below 38°). Both mono-specific time series $\Delta(\delta^{13}C_{rub})$ and $\Delta(\delta^{13}C_{sac})$ are very similar to each other, and a linear regression through a scatter plot of both data sets has a slope of ~ 0.99 – although the laboratory-based CIE for both species differs by a factor of nearly 2, implying that they should record distinctly different changes in δ^{13}C, if we accept that the carbonate ion concentration changes on glacial–interglacial timescales. For a deeper understanding of the ^{13}C cycle, we use the Solid Earth version of the Box model of the Isotopic Carbon cYCLE (BICYCLE-SE) to calculate how surface-ocean CO_3^{2-} should have varied over time in order to be able to calculate the potential offsets which would by caused by the CIE quantified in culture experiments. Our simulations are forced with atmospheric reconstructions of CO_2 and $\delta^{13}CO_2$ derived from ice cores to obtain a carbon cycle which should at least at the surface ocean be as close as possible to expected conditions and which in the deep ocean largely agrees with the carbon isotope ratio of dissolved inorganic carbon (DIC), $\delta^{13}C_{DIC}$, as reconstructed from benthic foraminifera. We find that both $\Delta(\delta^{13}C_{rub})$ and $\Delta(\delta^{13}C_{sac})$ agree better with changes in simulated $\delta^{13}C_{DIC}$ when ignoring the CIE than those time series which were corrected for the CIE. The combination of data- and model-based evidence for the lack of a role for the CIE in $\Delta(\delta^{13}C_{rub})$ and $\Delta(\delta^{13}C_{sac})$ suggests that the CIE as measured in laboratory experiments is not directly transferable to the interpretation of marine sediment records. The much smaller CIE-to-glacial–interglacial-signal ratio in foraminifera δ^{18}O, when compared to δ^{13}C, prevents us from drawing robust conclusions on the role of the CIE in δ^{18}O as recorded in the hard shells of both species. However, theories propose that the CIE in both δ^{13}C and δ^{18}O depends on the pH in the surrounding water, suggesting that the CIE should be detectable in neither or both of the isotopes. Whether this lack of role of the CIE in the interpretation of planktic paleo-data is a general feature or is restricted to the two species investigated here needs to be checked with further data from other planktic foraminiferal species.

1 Introduction

For a reconstruction of past changes in the ocean and in the carbon cycle, various variables are measured in microfossils obtained from marine sediment cores. Among the most widely used are the stable carbon and oxygen isotope ratios, δ^{13}C and δ^{18}O, from hard shells of planktic and ben-

thic foraminifera. Since the publication of the first stable isotope time series (Emiliani, 1955) a vast number of stable isotope records have been published and to a large part compiled in the World Atlas of late Quaternary Foraminiferal Oxygen and Carbon Isotope Ratios (Mulitza et al., 2022). One of the fundamental problems with the interpretation of foraminiferal isotope ratios is how and why a stable isotope signal was altered on its way from the seawater to the shell of living foraminifera. Are there vital and other effects necessary to be considered when interpreting the paleo-records (e.g. Bijma et al., 1999; Zeebe et al., 2008; Kimoto, 2015)?

The carbonate ion effect (CIE) is one of these potentially important effects that might alter the isotopic signal. The CIE implies that both $\delta^{13}C$ and $\delta^{18}O$ measured in hard shells of marine organisms undergo isotopic fractionation during calcite formation with the amplitude of the fractionation, among other factors, being a function of the carbonate ion concentration ($[CO_3^{2-}]$) of the surrounding seawater (Spero et al., 1997). The CIE has been found to be species-specific (Spero et al., 1999), ranging from -4.7×10^{-3} ‰ to -13.0×10^{-3} ‰ per µmol kg^{-1} of $[CO_3^{2-}]$ for $\delta^{13}C$ and between -1.4×10^{-3} ‰ and -4.5×10^{-3} ‰ per µmol kg^{-1} of $[CO_3^{2-}]$ for $\delta^{18}O$ in four planktic foraminifera. The CIE for $\delta^{13}C$ has been explained for *Orbulina universa*, a spinose, symbiont-bearing species, by the pH-related distribution of dissolved inorganic carbon (DIC) into its three species: CO_2, CO_3^{2-} and HCO_3^- (Wolf-Gladrow et al., 1999; Zeebe et al., 1999). The CIE on $\delta^{18}O$ is also explained by the CO_3^{2-}-related varying pH (Zeebe, 1999). These theories, however, were unable to base the full amplitudes found in experiments solely on this effect. The CIE is maybe the most prominent isotopic fractionation effect which has to be considered when interpreting the paleo-records, but others, e.g vital effects and dependency on light, temperature, pressure and shell size, have been put forward (e.g. Spero and Williams, 1988, 1989; Spero et al., 1991; Spero, 1992; Spero and Lea, 1993; Oppo and Fairbanks, 1989). The CIE is found to play a minor role when comparing late Holocene deep-ocean $\delta^{13}C$ in benthic foraminifera, with $\delta^{13}C$ of DIC ($\delta^{13}C_{DIC}$) (Schmittner et al., 2017) being responsible for -2.6×10^{-3} ‰ per µmol kg^{-1} of $[CO_3^{2-}]$ disturbance in the recorded signal. In a recent study focusing on the benthic species *Cibicidoides wuellerstorfi*, -3.0×10^{-3} ‰ per µmol kg^{-1} of $[CO_3^{2-}]$ has been obtained for the late Holocene (Nederbragt, 2023). Both studies also found in addition to the CIE that $\delta^{13}C_{benthic}$ was also partly controlled by other variables, mainly pressure (water depth) and temperature.

The CIE in planktic foraminifera is one of the reasons why the interpretation of the whole $\delta^{13}C$ cycle over glacial–interglacial timescales is still challenging. In a compilation of foraminiferal $\delta^{13}C$ measurements covering the past 150 kyr, Oliver et al. (2010) find relatively large disagreements between different planktic $\delta^{13}C$ records within a region compared to benthic records, consistent with large uncertainty

attributed to the estimation of $\delta^{13}C_{DIC}$ from planktic species. Since benthic compilations are less affected by the CIE, they should, however, robustly constrain deep-ocean changes in $\delta^{13}C_{DIC}$. A more recent compilation of benthic $\delta^{13}C$ was given in Lisiecki (2014). Furthermore, $\delta^{13}C$ of atmospheric CO_2 ($\delta^{13}CO_2$) is now available over the last 155 kyr (Eggleston et al., 2016a) from ice cores. So far, tight constraints on the change in surface-ocean $\delta^{13}C_{DIC}$ are missing from our understanding, but, in principle, this information should be recorded in the hard shells of planktic foraminifera, even if hidden under the CIE.

In this study, we therefore aim to construct a robust time series of orbital changes in surface-ocean $\delta^{13}C_{DIC}$ based on planktic foraminifera data. We compiled $\delta^{13}C$ data largely based on Mulitza et al. (2022) covering the last 160 kyr. In order to be able to apply any species-specific CIE corrections, we compile mono-specific isotope records on the widely abundant shallow-dwelling planktic foraminifera species *Globigerinoides ruber* (*G. ruber* or rub) and *Trilobatus sacculifer* (*T. sacculifer* or sac) into stacks. Due to their spatial distribution (Fraile et al., 2008), this species selection leads effectively to the construction of $\Delta(\delta^{13}C_{rub})$ and $\Delta(\delta^{13}C_{sac})$ stacks based on sediment core data from latitudes smaller than 40°, potentially informing us about mean changes of $\delta^{13}C_{DIC}$ on orbital timescales in the surface of the wider tropical ocean. Accompanied stacks of $\Delta(\delta^{18}O_{rub})$ and $\Delta(\delta^{18}O_{sac})$ from the same cores will add further information on the CIE in $\delta^{18}O$.

A first surface-ocean $\delta^{13}C$ stack based on data from *T. sacculifer* obtained from five equatorial Atlantic records has been constructed by Curry and Crowley (1987) without any knowledge on the CIE. Furthermore, Spero et al. (1999) used data from *G. ruber* and *T. sacculifer* from a single core in the Indian Ocean and the lab-based size of their species-specific CIE to deconvolve surface-ocean $[CO_3^{2-}]$. Here we will use our new mono-specific $\delta^{13}C$ stacks, which, due to the underlying number of records, have a much higher signal-to-noise ratio to test the robustness of their findings.

In the following, we will investigate the connection of $\delta^{13}C$ in the atmosphere and ocean in closer detail in order to improve our understanding of the ^{13}C cycle. The remainder of the article is structured as follows. Firstly (Sect. 2.1), we describe the construction of our mono-specific $\delta^{13}C$ anomaly stacks, $\Delta(\delta^{13}C_{rub})$ and $\Delta(\delta^{13}C_{sac})$ (and of the accompanied $\delta^{18}O$ anomalies). Some published benthic $\delta^{13}C$ data are also needed for our understanding (Sect. 2.2). For a deeper interpretation, the global isotope-enabled carbon cycle model, the Solid Earth version of the Box model of the Isotopic Carbon cYCLE (BICYCLE-SE) (Köhler and Munhoven, 2020), which has been proven to simulate glacial–interglacial (G-IG) in the carbon cycle reasonably well, is used. The model is briefly described in Sect. 2.3, including a completely revised parametrisation of the ^{13}C cycle. In Sect. 3.1, we discuss what we already know from data on the $\delta^{13}C$ cycle and the role the CIE might play. We then analyse the simulated $\delta^{13}C$

cycle in our model results in Sect. 3.2. This enables us to evaluate (Sect. 3.3) if our stacks, $\Delta(\delta^{13}C_{rub})$ and $\Delta(\delta^{13}C_{sac})$, are good representations of changes in $\delta^{13}C_{DIC}$ in the wider tropical surface ocean or if corrections such as the CIE need to be applied. Finally, we briefly discuss the CIE in $\delta^{18}O_{rub}$ and $\delta^{18}O_{sac}$ (Sect. 3.4) before we come to our conclusions (Sect. 4).

2 Methods

2.1 Constructing new mono-specific stacks from planktic foraminifera

2.1.1 Data source and age modelling

To construct time series of low-latitude $\delta^{13}C$ variations through the past 160 kyr, we selected 112 and 40 $\delta^{13}C$ records of the shallow-dwelling planktic foraminifera *G. ruber* and *T. sacculifer*, respectively, predominantly from the World Atlas of late Quaternary Foraminiferal Oxygen and Carbon Isotope Ratios (Mulitza et al., 2022). A list of the isotope records contributing to our stacks with relevant metadata, references to the original publications and data sources is provided in Table S1. In three sediment cores, time series from both *G. ruber* (white) and *G. ruber* (pink) contribute to our *G. ruber* stacks, while data from 22 cores contain mono-specific data from both *G. ruber* and *T. sacculifer*. All combined, our data selection is based on material from 127 sediment cores. The core sites cover a latitudinal range from 37.6° N to 36.7° S for *G. ruber* and from 32.8° N to 31.3° S for *T. sacculifer* in all major ocean basins (Fig. 1), although the contributions from individual cores (and therefore the latitudinal range) changed over time (Fig. 2c). Our age models are based on either radiocarbon ages or oxygen isotope stratigraphy or a combination of both methods. To calibrate radiocarbon ages, we first subtracted a simulated local reservoir age from the nearest grid box of the modelling experiments conducted for Marine20 (Butzin et al., 2020; Heaton et al., 2020a) and then calibrated the corrected radiocarbon age with the IntCal20 calibration curve (Reimer et al., 2020). For core sections with insufficient radiocarbon coverage or outside the radiocarbon dating range, ages were added through the visual alignment with the isotope stacks by Lisiecki and Raymo (2005) and Lisiecki and Stern (2016) using the software PaleoDataView (Langner and Mulitza, 2019). In a few cases, age models were derived by visual alignment with the oxygen isotope records of well-dated nearby cores. The details of the age model construction are available in the netCDF files of the age models in the corresponding PaleoDataView collection (Köhler and Mulitza, 2023). A continuous age model was then constructed with the age modelling software BACON (Blaauw and Christen, 2011). For each record, we produced an ensemble of 1000 time series by combining 1000 BACON-generated age models with 1000 down-core $\delta^{13}C$ and $\delta^{18}O$ series by adding a random value within the typical analytical 1σ-uncertainty of 0.05 % and 0.07‰ to each down-core $\delta^{13}C$ and $\delta^{18}O$ value, respectively. The resulting 1000 $\delta^{13}C$ and $\delta^{18}O$ time series were then interpolated to a time step of 1 kyr to calculate the mean and the standard deviation of the time series ensembles. The averaging of the individual ensemble members led to a considerable smoothing of the final time series.

2.1.2 Stacking of down-core isotope records

Although the size class used for stable isotope measurements can vary considerably among records, it is common practice to use a fairly constant shell size down-core to minimise size-related effects on both oxygen and carbon isotope ratios (e.g. Oppo and Fairbanks, 1989). To provide a common baseline, we corrected all isotope records by their individual mean values for the period from 21 to 19 kyr BP marked as Last Glacial Maximum (LGM) in various plots. To produce final isotope stacks, we averaged all corrected time series and calculated the standard error (SE) of the means at 1 kyr intervals. The final mono-specific stacks of both $\delta^{18}O$ and $\delta^{13}C$ anomalies based on *G. ruber* and *T. sacculifer* are plotted in Fig. 2a, b. The oxygen isotope stacks are also shown here to give a clear reference for G-IG changes: $\delta^{18}O$ has its maxima during peak glacial times and its minima during peak interglacials. In Sect. 3.4 we will come back to these data to discuss the CIE in $\delta^{18}O_{rub}$ and $\delta^{18}O_{sac}$. To test the extent to which the data distribution affects the stacks, we generated two versions of the stacks: one based on all records (Fig. 2a–d) and an alternative based only on records which contain both Terminations (T1 + T2; Fig. 2e–h). The stack counts (Fig. 2d, h) show that the two versions differ mainly in the younger half and that they are identical beyond 85 kyr BP. The latitudinal ranges in the younger half are slightly smaller for the compilations T1 + T2 than when all cores are compiled, but the mean latitudes of all cores are throughout the covered time window of the last 160 kyr in all cases (for both species and for both compilations) close to the Equator (Fig. 2d, g). This consistency in the mean latitude suggests that the incoming light which varied in its annual mean values between $\sim 420\,\mathrm{W\,m^{-2}}$ at the Equator and $\sim 330\,\mathrm{W\,m^{-2}}$ around latitudes of 40° (Laskar et al., 2004) should only marginally affect the isotopic fractionation (e.g. Spero et al., 1991).

2.2 Benthic $\delta^{13}C$

The focus of this study is the $\delta^{13}C$ of the surface ocean. However, for a rough comparison of $\delta^{13}C$ changes in the deep ocean, we rely on the published $\delta^{13}C$ stack constructed from six deep Pacific cores as contained in Lisiecki (2014). The six cores are all ODP cores (677, 846, 849, 1123, 1143 and 1208) from between 2700 and 3500 m water depth, located between 42° S and 36° N. The deep Pacific $\delta^{13}C$ stack should cover the most-depleted end member of the marine $\delta^{13}C$ cy-
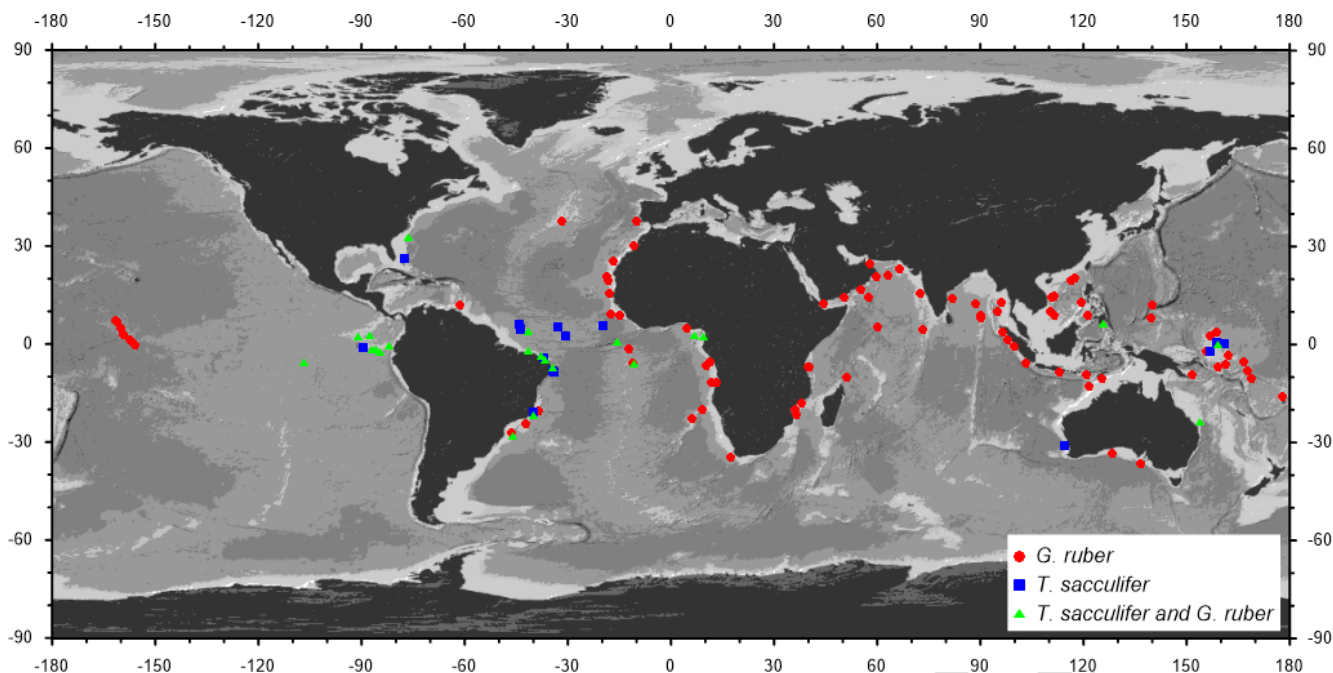
Figure 1. Location of the 127 sediment cores from which data have been compiled for this study. Data from the planktic species *G. ruber* have been included in 87 cores, and in 18 cores data from *T. sacculifer* have been included, while 22 cores provide mono-specific data from both species.

cle (Fig. 3d) and should give some indication how δ^{13}C in the deep ocean is performing in our simulations. More details on the stack are found in Lisiecki (2014).

2.3 The carbon cycle model BICYCLE-SE

2.3.1 Brief model description

At the core of BICYCLE – the Box model of the Isotopic Carbon cYCLE – sits an ocean (O) with 10 boxes and a terrestrial biosphere consisting of 7 boxes (B) together with a 1-box atmosphere (A), in which the concentration of carbon (as DIC in the ocean, as pCO$_2$ in the atmosphere and as organic carbon in the biosphere) and both of the isotopes δ^{13}C and Δ^{14}C are traced (Köhler et al., 2005). Furthermore, in the ocean alkalinity, PO$_4^{3-}$ as a macro-nutrient and O$_2$ are represented. From the two variables in the marine carbonate system (DIC and alkalinity), all other variables (CO$_2$, HCO$_3^-$, CO$_3^{2-}$ and pH) are calculated according to Zeebe and Wolf-Gladrow (2001) with updates of the dissociation constants pK$_1$ and pK$_2$ (Mojica Prieto and Millero, 2002). The 10 ocean boxes distinguish 100 m deep equatorial (or wider tropical) surface waters in the Atlantic and Indo-Pacific from 1000 m deep surface-ocean boxes in the high latitudes (North Atlantic, Southern Ocean and North Pacific). In the model, wider tropical boxes range from 40° S to 40° N in the Indo-Pacific and to 50° N in the Atlantic, rather similar to the latitudinal coverage of the sediment cores from which $\Delta(\delta^{13}$C$_{\mathrm{rub}})$ and $\Delta(\delta^{13}$C$_{\mathrm{sac}})$ have been constructed.

Deep-ocean boxes represent all waters below 1 km in the three basins: Atlantic, Southern Ocean and Indo-Pacific. In the equatorial regions the waters between 100 and 1000 m depth are described by intermediate boxes. The terrestrial biosphere (Köhler and Fischer, 2004) distinguishes C$_3$ and C$_4$ photosynthesis of grasses and trees and soil carbon with different turnover times of up to 1000 years.

The model extension towards the version BICYCLE-SE used here, which can take care of solid Earth processes, is sketched in Fig. 4. The main improvement documented in detail in Köhler and Munhoven (2020) is the implementation of a sediment module, which captures early diagenesis in an 8 cm deep sedimentary mixed layer (M), under which numerous historical layers are implemented. In effect, we now simulate the subsystem of the global carbon cycle consisting of atmosphere, ocean, terrestrial biosphere and sedimentary mixed layer (AOBM) within BICYCLE-SE. In each of the three ocean basins (Atlantic, Southern Ocean and Indo-Pacific) the pressure-dependent carbonate system is calculated for every 100 m water depth, and, depending on the over- or undersaturation of the carbonate ion concentration, CaCO$_3$ is either accumulated or dissolved. The parametrisation and realisation of the sedimentary processes directly follow Munhoven and François (1996) and Munhoven (1997). The carbon isotopes in the sedimentary mixed layer are only followed in aggregated boxes (one for each of the three ocean basins).
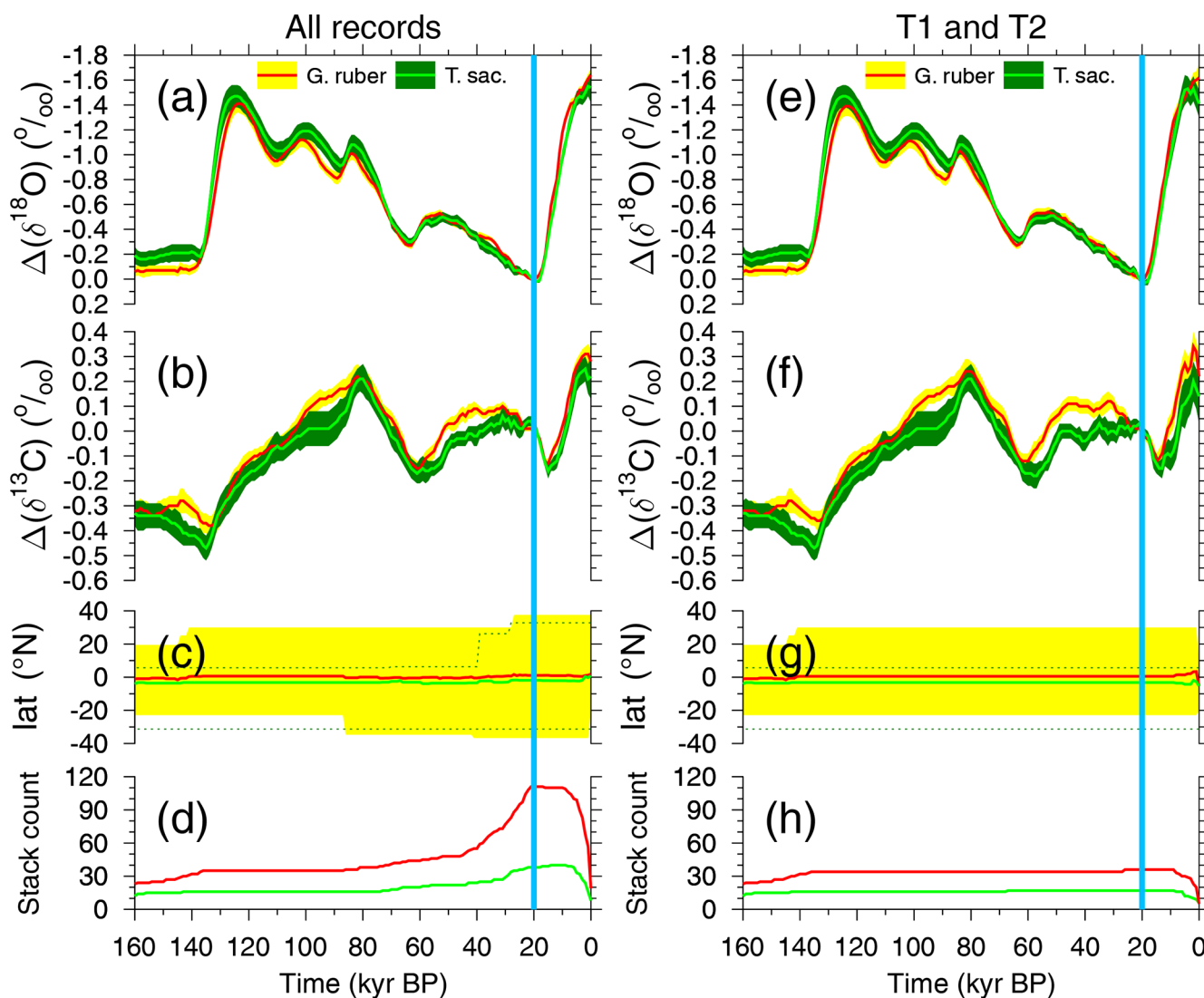
Figure 2. Stacks of anomalies in (**a, e**) $\delta^{18}O$ and (**b, f**) $\delta^{13}C$ from the planktic species *G. ruber* and *T. sacculifer* across the last 160 kyr. Mean anomalies (± 1 SE) are calculated with respect to the mean of 21–19 kyr BP (vertical blue band). Details of underlying data are found in Table S1. (**c, g**) Latitudinal distribution of cores contributing to the stack (mean and full range) and (**d, h**) stack count. Either data from all cores for each species are compiled (**a–d**) or (**e–h**) they are compiled from a reduced core selection, in which contributing cores cover both Termination 1 and 2 (T1 + T2).

Equipping BICYCLE with a process-based sediment module enables the revised model version, BICYCLE-SE, to address questions related to changes in solid Earth carbon fluxes in detail and in the long term. Roughly speaking, the following processes are considered. CO_2 outgassing from volcanoes on land, hot-spot island volcanoes and mid-ocean ridge (MOR) hydrothermal activity is realised as partly being dependent on the changing sea level. Coral reef growth is a known shallow-water carbonate sink, which to some extent also follows sea level rise. The weathering of silicate or carbonate rocks on land consumes different amounts of atmospheric CO_2, with both leading to bicarbonate fluxes into the ocean. These solid Earth processes are not directly coupled with each other. Their implementation in the model might therefore lead to temporal offsets in various variables, to which the sediment module might react in a carbonate compensation feedback. Further details on the model and the time-dependent forcing are found in Köhler and Munhoven (2020). Part of this brief model description has been taken from Köhler (2020).

2.3.2 Complete formulation of the ^{13}C cycle in BICYCLE-SE

The following isotopic fractionations are now considered in the BICYCLE-SE model. For this study the whole $\delta^{13}C$ cy-
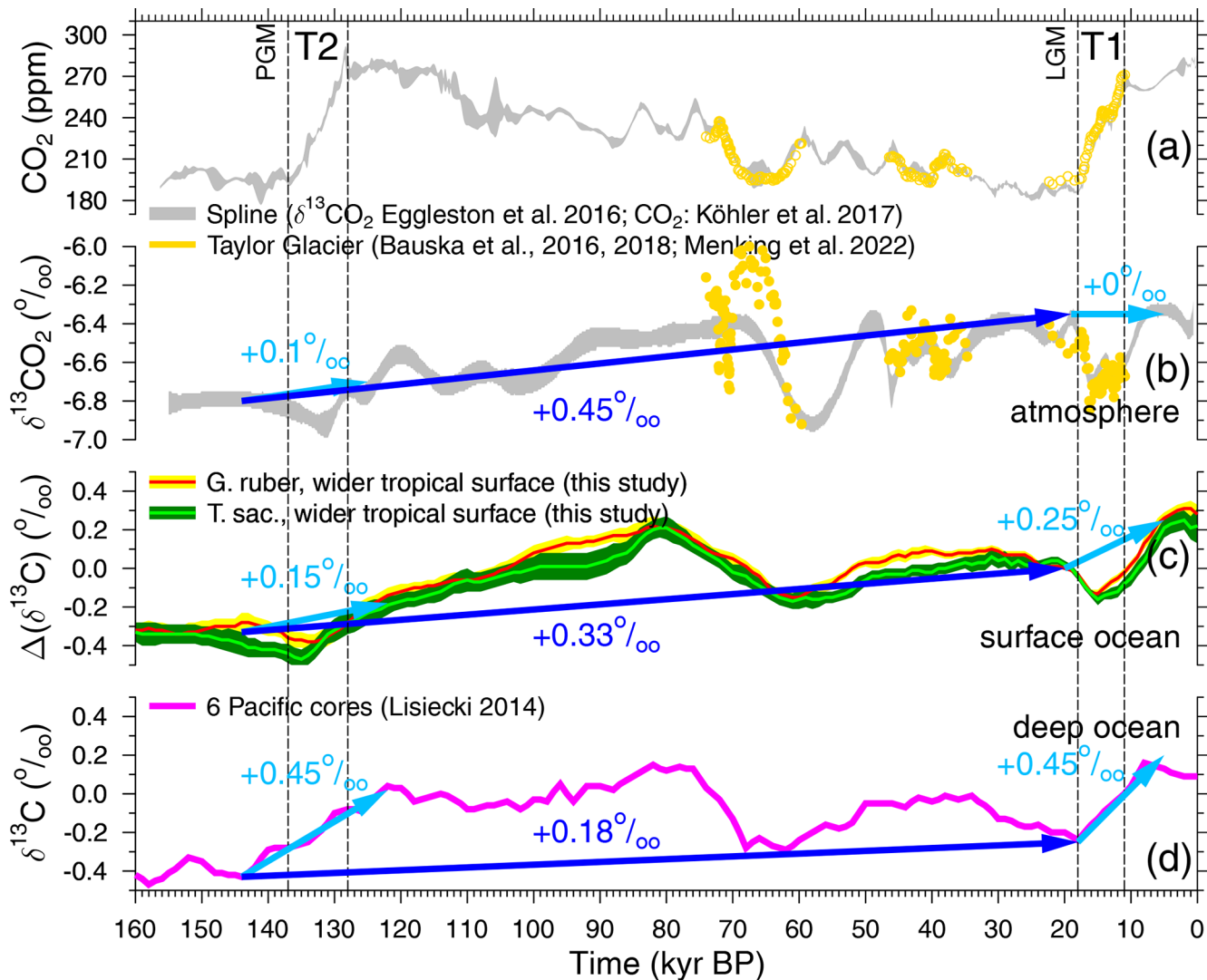
Figure 3. Carbon cycle time series of the last 160 kyr, including the Penultimate Glacial Maximum (PGM) and the Last Glacial Maximum (LGM) and Terminations 1 and 2 (T1 and T2). Spline of atmospheric CO_2 **(a)** and $\delta^{13}CO_2$ **(b)** based on data from various ice cores (grey, $\pm 1\sigma$ around the mean; Köhler et al., 2017a; Eggleston et al., 2016a) and highly resolved recent data from the "horizontal ice core" approach in Taylor Glacier (yellow; Bauska et al., 2016, 2018; Menking et al., 2022b). **(c)** $\Delta(\delta^{13}C_{rub})$ and $\Delta(\delta^{13}C_{sac})$ averaging signals in the wider tropical surface ocean (this study, largely based on Mulitza et al., 2022). **(d)** Deep-ocean $\delta^{13}C$ from benthic foraminifera stacked from six Pacific cores (Lisiecki, 2014).

cle has been revised. While isotopic fractionations are given here in the $\varepsilon_{(A-B)}$-notation (in ‰) they are implemented after Zeebe and Wolf-Gladrow (2001) in the model as fractionation factors $\alpha_{(A-B)}$. Both are related following

$$\varepsilon_{(A-B)} = 1000 \cdot (\alpha_{(A-B)} - 1). \tag{1}$$

Furthermore, $\alpha_{(A-B)}$ is related to $\delta^{13}C$ in reservoirs A and B:

$$\alpha_{(A-B)} = \frac{\delta^{13}C_A + 1000}{\delta^{13}C_B + 1000}. \tag{2}$$

There is no convention if the initial or final reservoir is given as A or B here; however, here, A is always the final reser-

voir and B is the initial reservoir of the fractionation process. In some cases, a specific process instead of two reservoirs is mentioned in the subscript, e.g. $\varepsilon_{(a \to o)}$ and $\varepsilon_{(o \to a)}$ for the atmosphere–ocean gas exchange, for which not only the two different reservoirs but also the direction of the flux play a role in the size of the isotopic fractionation. In that case, the quantified fractionation implies an isotopic depletion connected with the related process for $\varepsilon < 0$‰.

Air–sea gas exchange. Using the measurements from Zhang et al. (1995) we formulate, following in most parts Marchal et al. (1998), for the isotopic fractionation during gas exchange to consist of contributions
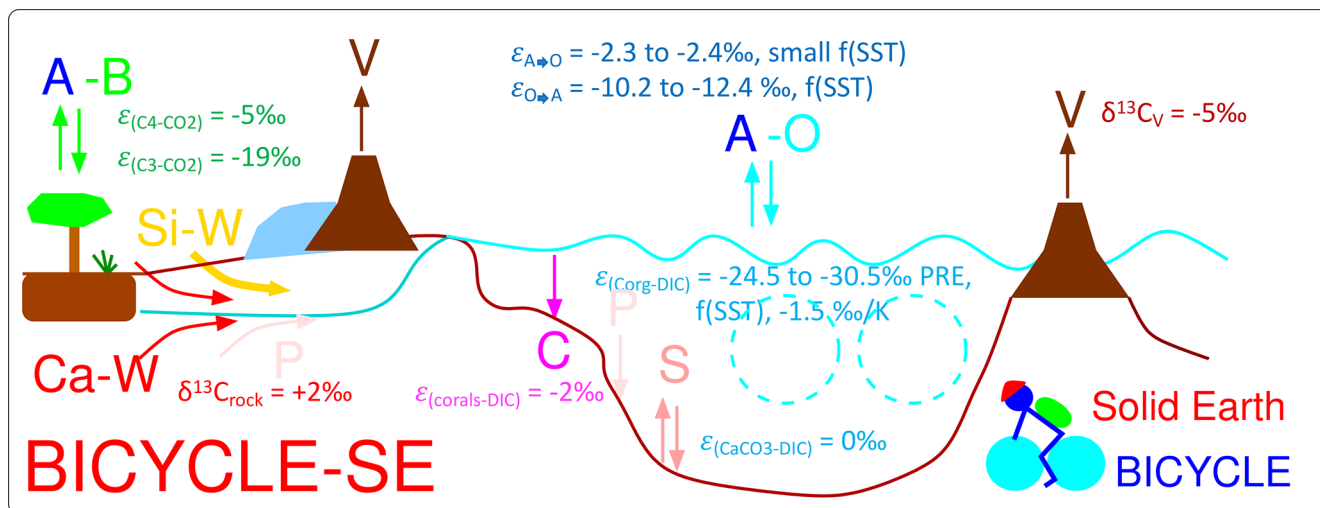
Figure 4. Sketch of the Box model of the isotopic carbon cycle, version solid Earth (BICYCLE-SE), modified from Köhler and Munhoven (2020). V is the outgassing of CO_2 from volcanoes on land potentially and temporally overlain by land ice and from hot-spot island volcanoes (and mid-ocean ridges, not shown) influenced by the changing sea level. C is shallow-water carbonate deposition due to coral reef growth. Si-W is silicate weathering, and Ca-W is carbonate weathering, with different sources of C but both delivering HCO_3^--ions into the ocean. P is the PO_4^{3-} riverine input and sedimentary burial, and S is the $CaCO_3$ sedimentation and dissolution. A–B is the atmosphere–biosphere exchange of CO_2, and A–O is the atmosphere–ocean exchange of CO_2. The cyan-coloured broken circles mimic the two overturning cells in the Atlantic and Indo-Pacific oceans. The isotopic fractionation ε during exchange processes, or the prescribed $\delta^{13}C$ of external fluxes, is given, summarising the parametrisation of the ^{13}C cycle within the model.

from equilibrium (α^{eq}) and kinetic (α^k) fractionation ($\alpha^{total} = \alpha^{eq} \cdot \alpha^k$). For the atmosphere-to-ocean CO_2 flux, a temperature-dependent equilibrium fractionation of $\varepsilon_{a \to o}^{eq} = \varepsilon_{(aq-g)}^{eq} = -1.31 + 0.0049 \cdot T_C$ between dissolved (aq) and gaseous (g) CO_2 and a $\varepsilon_{a \to o}^{k} = -1.08‰$ is used. Note that $\varepsilon_{a \to o}^{k}$ differs by $-0.2‰$ from $\varepsilon_{o \to a}^{k} = -0.88‰$ for the ocean-to-atmosphere flux, a necessary correction already given in Zhang et al. (1995) but to our knowledge only rarely applied. For the reverse ocean-to-atmosphere flux we use the equilibrium fractionation $\alpha_{o \to a}^{eq} = \alpha_{(aq-DIC)}^{eq} = \sum_i f_i \alpha_{(aq-i)}$, with f_i being the relative shares of CO_2, HCO_3^- and CO_3^{2-} in DIC in the representative ocean box. Furthermore, from the available measurements in Zhang et al. (1995), we derive $\alpha_{(aq-HCO_3^-)} = \frac{\alpha_{(aq-g)}}{\alpha_{(HCO_3^- - g)}}$, $\alpha_{(aq-CO_3^{2-})} = \frac{\alpha_{(aq-g)}}{\alpha_{(CO_3^{2-} - g)}}$ and $\alpha_{(aq-CO_2)} = 1$ using $\varepsilon_{(CO_3^{2-} - g)} = 7.22 - 0.052 \cdot T_C$ and $\varepsilon_{(HCO_3^- - g)} = 10.78 - 0.114 \cdot T_C$, with T_C being the sea surface temperature in °C.

Marine biology. The preindustrial marine export production of organic carbon at 100 m water depth is set to 10 PgC yr^{-1} (which in the model can increase in glacial periods due to iron fertilisation in the Southern Ocean up to 13 PgC yr^{-1}; Fig. S1d) with a fixed molar rain ratio of organic C:$CaCO_3$ of 10 : 1. Existing data on fractionation during marine organic matter production (marine photosynthesis) are rather weak in determin-

ing if and how it depends on CO_2 (Young et al., 2013; Brandenburg et al., 2022; Liu et al., 2022). Furthermore, as discussed in Brandenburg et al. (2022), some species might contain so-called carbon concentrating mechanisms and use not CO_2 but HCO_3^- as the source of their carbon, in which case a completely different isotopic fractionation during marine photosynthesis ($\varepsilon_{(C_{org}-DIC)}$) would follow. We base our initial formulation of $\varepsilon_{(C_{org}-DIC)}$ on the data compilation of $\delta^{13}C_{POC}$ in Verwega et al. (2021), who found a dependency on latitude. Using average preindustrial $\delta^{13}C_{DIC}$ of $+2.5‰$ (Schmittner et al., 2013) as a starting value and the $\delta^{13}C_{POC}$ in Verwega et al. (2021) of $-22‰$, $-24‰$ and $-28‰$ for low, high northern and high southern latitudes, respectively, and approximating $\varepsilon_{(C_{org}-DIC)} \approx \delta^{13}C_{POC} - \delta^{13}C_{DIC}$, we come up with the following isotopic fractionation $\varepsilon_{(C_{org}-DIC)}$ of $-24.5‰$, $-26.5‰$ and $-30.5‰$ accordingly. This approximation is motivated by the high uncertainties in $\delta^{13}C_{POC}$ as documented in Verwega et al. (2021).

The spread in $\delta^{13}C_{POC}$ in the data of Verwega et al. (2021) is huge, ranging from $-15‰$ to $-35‰$. Furthermore, they confirmed the finding of earlier studies (Young et al., 2013; Lorrain et al., 2020) that $\delta^{13}C_{POC}$ becomes much more depleted over time than what is explainable by the ^{13}C Suess effect (Keeling, 1979). Between 1960 and 2010 $\delta^{13}C_{POC}$ decreased by about $3 \pm 4‰$. The Suess effect shows a decrease in atmo-

spheric $\delta^{13}CO_2$ of about 1.5‰ during that time (Rubino et al., 2013), and it is known that in the ocean the Suess effect is decreasing with depth (Eide et al., 2017). At the same time, the global mean temperature rose by about 0.8 K (Rohde and Hausfather, 2020). This shift in $\delta^{13}C_{POC}$ is probably caused by a shift in the composition of the phytoplankton communities. We therefore use the values derived in the previous paragraph from Verwega et al. (2021) as our preindustrial parameter values of $\varepsilon_{(C_{org}-DIC)}$, to which we add a temperature-dependent part of $-1.5‰$ for any K the sea surface temperature in the relevant surface-ocean box disagrees with from its preindustrial value. The assumed value fits in the range of recent temperature-dependent $\delta^{13}C_{POC}$ found in Verwega et al. (2021) and has been obtained by tuning to simulate $\delta^{13}CO_2$ at preindustrial times to be similar to its values at the LGM, as seen in the ice core data (Fig. 3b). This leads to $\varepsilon_{(C_{org}-DIC)}$ at the LGM of $-19.3‰$, $-20.4‰$ and $-24.4‰$ for low, high northern or high southern latitudes, respectively.

Data are also rather uncertain for the isotopic fractionation during the formation of $CaCO_3$. We assume, in agreement with Buitenhuis et al. (2019), that 65 % of the $CaCO_3$ exported in the abyss consists of aragonite and 35 % of calcite. Calcite is either produced by coccolithophores or planktic foraminifera. Some coccolithophore species suggest an enrichment, while others suggest a depletion in $\delta^{13}C$ in their shells with respect to $\delta^{13}C_{DIC}$ in the surrounding water (Ziveri et al., 2003). For planktic foraminifera, the CIE is one of various possible processes of isotopic fractionation hypothesised to occur during hard-shell formation (Bijma et al., 1999; Zeebe et al., 2008; Kimoto, 2015). Isotopic fractionation factors are in comparison to $\varepsilon_{(C_{org}-DIC)}$ rather small and, in the case of the CIE, species-specific (Spero et al., 1999). We therefore choose in the model to set the fractionation during calcite production to be neutral with respect to ^{13}C, thus $\varepsilon_{(cal-DIC)} = 0‰$, but we will consider the CIE in post-processing when comparing simulations with reconstructions. For simplicity and due to missing further evidence for fractionation during aragonite production, $\varepsilon_{(ara-DIC)}$ was also kept at 0‰. More generally, we keep $\varepsilon_{(CaCO_3-DIC)} = 0‰$.

The shallow-water sink of carbonate in corals is assumed to have a $\delta^{13}C$ that follows after an isotopic fraction of $\varepsilon_{(corals-DIC)} = -2‰$ from the $\delta^{13}C$ of the DIC in the surface waters. This value is based on a combination of recent data, paleo-data from the Great Barrier Reef and insights from simulations (Linsley et al., 2019; Felis et al., 2022).

Terrestrial biosphere: On land, isotopic fractionation is only assumed to occur during photosynthesis, with $\varepsilon_{(C_3-CO_2)} = -19‰$ and $\varepsilon_{(C_4-CO_2)} = -5‰$ for C_3 (all woody plants and some grasses) and C_4 (some other grasses) photosynthesis, respectively (Vogel, 1993; Lloyd and Farquhar, 1994).

External fluxes to the AOBM subsystem: The volcanic CO_2 outgassing flux is assumed to have a fixed $\delta^{13}C$ signature ($\delta^{13}C_V$) of $-5.0‰$, the typical mean value for volcanic outgassing (e.g. Deines, 2002; Roth and Joos, 2012), but note that the uncertainty is $\pm 3‰$.

From the two weathering fluxes based on either silicate or carbonate rocks, only the latter has a contribution which brings new carbon into the system. Here, 50 % of the carbon that is entering the ocean as bicarbonate (the weathering product) has a $\delta^{13}C$ signature ($\delta^{13}C_{rock}$) of $+2‰$, which is identical to the most likely $\delta^{13}C$ values in carbonate rocks formed during the Phanerozoic (Bachan et al., 2017). The carbon for the other half of the carbonate weathering flux and for all of the silicate weathering flux is assumed to come from CO_2 in the soil environment. We therefore assume that this CO_2 is dominated by soil respiration fluxes; therefore, a $\delta^{13}C$ signature that corresponds to the mean value of the two soil carbon boxes is assumed here.

To balance the inflow of ^{13}C via volcanism and weathering, the model has been tuned for long-term stable mean $\delta^{13}C$ values in the AOBM subsystem by the following sink: about 6 % of the organic carbon that is exported from the surface boxes into the abyss is assumed to be lost in the sediment. Note that this number has been tuned with the previous version of the ^{13}C cycle in operation (Köhler and Munhoven, 2020), but it has not been revised thereafter.

2.3.3 Simulation setup and scenarios

The BICYCLE-SE model simulates the global carbon cycle as a function of changing time-dependent physical boundary conditions (forcing), which are nearly identical to the simulations published in Köhler and Munhoven (2020) and which are also described in that study in detail. Briefly, ocean circulation is prescribed from modern data of the WOCE experiment, while its main temporal changes are restricted to (a) the AMOC, which is reduced from modern/interglacial 16 to 10 Sv during glacial periods (Fig. S1b), and (b) Southern Ocean (SO) vertical deep mixing, which is a function of SO sea surface temperature (Fig. S1c). Ocean and land temperatures are prescribed from reconstructions (Fig. S1e), and ocean salinity is varied as a function of the prescribed sea level (Fig. S1a). Additionally, aeolian iron input in the SO is assumed to follow dust fluxes measured in Antarctic ice cores, which might change marine biology in the SO from an iron-limited to an iron-unlimited regime, increasing glacial export production of organic matter to the deep ocean (Fig. S1d). The standard scenario used here, SEi, is, apart from the revised $\delta^{13}C$ cycle, nearly identical to the scenario SE in Köhler and Munhoven (2020). The only difference here

is that in the application we revised the applied equatorial sea surface temperature (SST). It has been based in previous applications on changes in planktic $\delta^{18}O$ in only one ODP record. Now we use the SST stack from Barth et al. (2018), which is based on a compilation of SSTs from 15 non-polar sediment cores. This leads to only minor changes in atmospheric CO_2 of less than 5 ppm, but it is important for the ^{13}C cycle and its temperature dependencies (isotopic fractionation during atmosphere–ocean gas exchange and during carbon uptake by the marine biology). Simulations are started from interglacial conditions around 210 kyr BP. Scenario SEi0 is only performed to illustrate how the implementation of the temperature dependency in $\varepsilon_{(C_{org}-DIC)}$ improves the simulated ^{13}C cycle, illustrated by plotting atmospheric $\delta^{13}CO_2$ against data in Fig. 5b.

Simulated changes in the atmospheric record are already not too far away from the reconstructions in scenario SEi, especially in CO_2 (Fig. 5a). However, to bring the carbon cycle in the atmosphere and the surface ocean as close to the reconstructions as possible, we perform additional simulations in which the atmospheric $\delta^{13}CO_2$ alone (scenario C1) or together with atmospheric CO_2 (scenario C1CO2) is forced by the reconstructions. Here, we use the data splines as plotted in Fig. 3a, b (Eggleston et al., 2016a; Köhler et al., 2017a) and ignore the higher resolved data from Taylor Glacier, since these more abrupt changes in $\delta^{13}CO_2$ are either covered to a large extent during the last 50 kyr in the dynamics of the spline (Bauska et al., 2016, 2018) or are probably not recorded in our marine sediment records around 70 kyr BP (Menking et al., 2022b). This implies that internally calculated fluxes are overwritten by changes that are necessary to keep the simulated atmospheric carbon variables identical to the reconstructions. This approach is typically applied in CO_2-concentration-driven present-day or future ocean carbon cycle simulations (e.g. Hauck et al., 2020). It has already been used in BICYCLE-SE for ^{14}C to obtain radiocarbon in the surface ocean as close to the data as possible during the construction of the most recent marine radiocarbon calibration curve Marine20 (Heaton et al., 2020b) and subsequent studies (Köhler et al., 2022). However, since atmospheric CO_2 and $\delta^{13}CO_2$ are normally prognostic variables of the model and their calculated changes should be derived from the model's differential equations followed by a proper integration scheme, this approach slightly violates the mass conservation. It nevertheless guarantees that simulated surface-ocean variables of the carbon cycle within the model realm are as consistent as possible with the atmospheric reconstructions. An overview of the applied simulation scenarios is compiled in Table 1.

2.4 Data analysis

Linear regression was performed with the software MATLAB (The MathWorks Inc., 2023). The uncertainties of the fits are approximated by root-mean-square errors calculated after $s = \sqrt{\frac{1}{n}\sum_{i=1}^{n}(y_i - f_i)^2}$, with f_i being the calculated values according to the linear regression equations. In cases in which the uncertainties in both variables should be considered, we used the function "linfitxy", version 1.2.0.0 (Browaeys, 2023). The frequency analysis was performed using R (R Core Team, 2023), including the function "coh" from the R package seewave, version 2.2.3, calculating coherence.

3 Results and discussion

3.1 Overview on ^{13}C cycle changes over the last 160 kyr

Reconstructed changes in the late Quaternary carbon cycle are still not completely understood. The ice cores give us a precise picture of atmospheric CO_2 (Bereiter et al., 2015; Köhler et al., 2017a) (Fig. 3a), which in the meantime has also been met reasonably well with various different carbon cycle models (e.g. Menviel et al., 2012; Ganopolski and Brovkin, 2017; Khatiwala et al., 2019; Köhler and Munhoven, 2020). These findings suggest that the main processes responsible for the observed changes on orbital timescales might indeed have been identified, although results are to some extent model-dependent and improvements in details are certainly necessary.

The corresponding atmospheric $\delta^{13}CO_2$, now available over the last 155 kyr (Eggleston et al., 2016a), is, however, still waiting for a process-based interpretation of all its features (Fig. 3b). Since $\delta^{13}CO_2$ helps to pinpoint processes responsible for CO_2 changes, any simulation that is able to explain one without the other might need to be interpreted with caution. Models suggest that especially physical and biological processes in the Southern Ocean processes robustly influence $\delta^{13}CO_2$, while the impact of the Atlantic meridional overturning circulation (AMOC) on $\delta^{13}CO_2$ seems to be model-dependent (Menviel et al., 2015). Consequently, the abrupt drop in $\delta^{13}CO_2$ at the onset of Termination 1 (T1) (Smith et al., 1999; Schmitt et al., 2012) is nowadays understood to be caused by marine processes, while subsequent $\delta^{13}CO_2$ changes during T1 and its recovery during the Holocene to LGM-like values were potentially related to a mixture of oceanic and terrestrial processes (Köhler et al., 2005; Bauska et al., 2016).

Two largely unexplained features stand out in the 155 kyr $\delta^{13}CO_2$ record. Firstly, there is a long-term trend of $+0.45\%_o$ from the Penultimate Glacial Maximum (PGM) and the Last Glacial Maximum (LGM). When first discovered (Schneider et al., 2013), it was hypothesised that changes in the isotopic composition of solid Earth fluxes or of their intensities or long-term peat build-up might be responsible for them. Secondly, a $0.5\%_o$ deep and nearly 20 kyr long minimum centred around 58 kyr BP happened, rather uncorrelated with CO_2 changes. Eggleston et al. (2016a) hypothesise that the $\delta^{13}CO_2$ minimum might have been partially caused by a change in ocean stratification between Marine Isotope
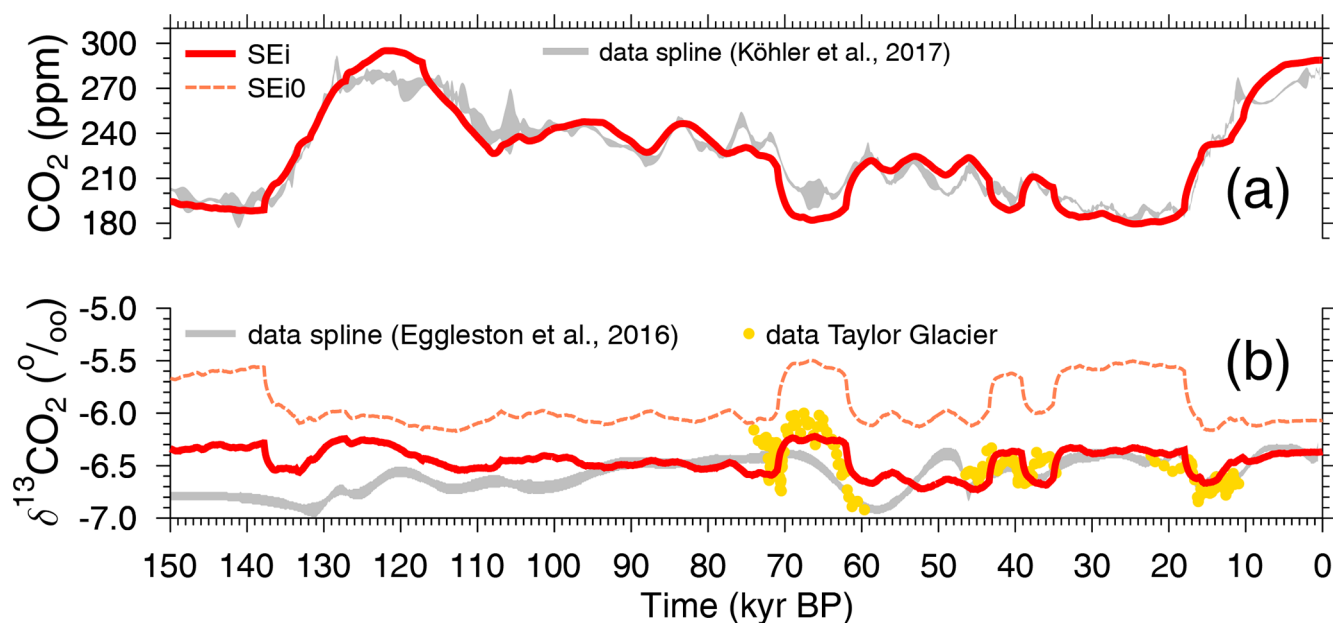
Figure 5. Simulation results and comparison to data splines for **(a)** atmospheric CO_2 and **(b)** atmospheric $\delta^{13}CO_2$. Results for scenario SEi (standard) and SEi0 are shown. The latter differs from the standard run by a lack of temperature dependency in $\varepsilon_{(C_{org}-DIC)}$.

Table 1. Overview of simulation scenarios.

Name	Description
SEi	Standard run for BICYCLE-SE with updated ^{13}C cycle
SEi0	Similar to SEi, but without temperature-dependent contribution to $\varepsilon_{(C_{org}-DIC)}$
C1	Similar to SEi, but atmospheric $\delta^{13}CO_2$ is prescribed from data (Eggleston et al., 2016a)
C1CO2	Similar to SEi, but atmospheric records ($\delta^{13}CO_2$, CO_2) are prescribed from data (Eggleston et al., 2016a; Köhler et al., 2017a)

Stage (MIS) 4 and MIS 3, allowing a different amount of isotopically light carbon to be stored in the deep ocean. Recently, high-resolution data of $\delta^{13}CO_2$ from Taylor Glacier covering 74 to 59.5 kyr BP, including MIS 4 and the drop into the $\delta^{13}CO_2$ minimum, have been published (Menking et al., 2022b), showing more variability and, between 66 and 60 kyr BP with $-1\,‰$, a change twice as large as that previously contained in the smoothed record of Eggleston et al. (2016a). Menking et al. (2022b) also first performed model simulations in order to understand which processes might be responsible for the reconstructed changes in the carbon cycle. However, to our knowledge, none of the ideas put forward in Schneider et al. (2013) for the long-term trend in $\delta^{13}CO_2$ have so far been convincingly and successfully verified with carbon cycle model simulation. Furthermore, 400–500 kyr variability in $\delta^{13}C$ related to slow eccentricity changes found throughout the Cenozoic (e.g. Pälike et al., 2006; Russon et al., 2010; Ma et al., 2011; Wang et al., 2014; Paillard, 2017) might be superimposed on faster variations, making a process-based understanding of observed changes in $\delta^{13}CO_2$ even more challenging.

Sediment cores covering the Anthropocene clearly show that the $\delta^{13}C$ of *G. ruber* and *T. sacculifer* shells ($\delta^{13}C_{rub}$ and $\delta^{13}C_{sac}$) faithfully reflects changes in $\delta^{13}C_{DIC}$ caused by the $\delta^{13}C$ Suess effect (Al-Rousan et al., 2004; Black et al., 2011), albeit with a notable offset. This offset might be influenced by the CIE (e.g. Spero et al., 1997), light intensity (e.g. Spero et al., 1991) and the size of the foraminiferal shells (e.g. Oppo and Fairbanks, 1989). Our new mono-specific stacks from the wider tropical surface ocean of $\Delta(\delta^{13}C_{rub})$ and $\Delta(\delta^{13}C_{sac})$ (Fig. 3c) contain a G-IG rise of 0.25 ‰ across T1 but of only 0.15 ‰ across T2, while atmospheric $\delta^{13}CO_2$ at the same time rose by 0.1 ‰ (T2) or stayed constant (T1) (Fig. 3b), showing local minima during terminations in both records. Deep-ocean benthic $\delta^{13}C$ (Fig. 3d) is approximated here by a stack from six deep Pacific cores (Lisiecki, 2014), which contains a G-IG rise of 0.45 ‰ across both T1 and T2. This value is on the upper end of the 95 % confidence interval of compilations of marine $\delta^{13}C$ changes across T1 (Peterson et al., 2014; Peterson and Lisiecki, 2018), which suggests a representation of global ocean-wide changes. The marine time series, both from the surface ocean and the deep ocean, also contain wide and deep minima around 60 kyr BP, simi-

larly to the smoothed atmospheric $\delta^{13}CO_2$ data of Eggleston et al. (2016a) but differently to the more highly resolved Taylor Glacier $\delta^{13}CO_2$ of Menking et al. (2022b). Furthermore, all marine $\delta^{13}C$ data, similarly to the atmospheric $\delta^{13}CO_2$, contain a long-term rise from the PGM to the LGM (about $+0.33\%_0$ in the wider tropical surface ocean and $+0.18\%_0$ in the deep Pacific; Fig.3), which might be potentially connected to the 400–500 kyr variability.

Before we start with a deeper model-based interpretation of the ^{13}C cycle, we have a closer look at our new isotope stacks. The size of the CIE as detected from laboratory experiments in both species differs by a factor of nearly 2: a change of $-0.0089\%_0$ and $-0.0047\%_0$ in $\delta^{13}C$ per μmol kg^{-1} of $[CO_3^{2-}]$ for *G. ruber* and *T. sacculifer*, respectively, and a change of $-0.0022\%_0$ and $-0.0014\%_0$ in $\delta^{18}O$ per μmol kg^{-1} of $[CO_3^{2-}]$ for *G. ruber* and *T. sacculifer*, respectively (Spero et al., 1999). Therefore, if the CIE plays a role in how the isotopes of the surface ocean are recorded in the foraminifera shells on orbital timescales, then the two mono-specific time series in both $\delta^{13}C$ and $\delta^{18}O$ should differ. At first glance (Fig. 2a, b) the time series are remarkable similar. A more quantitative evaluation is obtained by calculating the linear regression from scatter plots when results based on one species are plotted against those of the other. Doing so (Fig. 6) reveals for $\delta^{13}C$ that, on average, changes are identically recorded in both species. In other words, the linear slope of $\Delta(\delta^{13}C_{rub})$ against $\Delta(\delta^{13}C_{sac})$ is 0.98 ($r^2 = 0.95, s = 0.04\%_0$), or 0.99 ± 0.03 ($r^2 = 0.95$) when considering the uncertainties of our stack during regression. For $\delta^{18}O$ the agreement is only slightly worse: the regression slope of $\delta^{18}O_{rub}$ against $\delta^{18}O_{sac}$ is 0.96 ($r^2 = 0.96, s = 0.09\%_0$), or 0.98 ± 0.01 ($r^2 = 0.96$) with uncertainties. Since $\Delta(\delta^{13}C_{rub})$ and $\Delta(\delta^{13}C_{sac})$ are on average recording virtually the same changes, it is difficult to image how the species-specific CIE can play a role here. Due to the small amplitudes of the CIE in $\delta^{18}O$, it is as yet inconclusive if the CIE plays a role for $\Delta(\delta^{18}O_{rub})$ versus $\Delta(\delta^{18}O_{sac})$.

3.2 Simulated $\delta^{13}C$ cycle using the BICYCLE-SE model

General dynamics of the global carbon cycle in the BICYCLE-SE model have been analysed in detail in Köhler and Munhoven (2020). We focus here on the revised $\delta^{13}C$ cycle but see how atmospheric CO_2 in scenario SEi meets the ice core data in Fig. 5a. Note that some analysis of $\delta^{13}C$ in the precursor model BICYCLE without solid Earth contributions has been described in Köhler et al. (2010), who showed that the model misses variations in $\delta^{13}C$ related to periodicities longer than 100 kyr.

Atmospheric $\delta^{13}CO_2$ (Eggleston et al., 2016a) is met by the results from scenario SEi only roughly, including some millennial-scale variations around 50–30 kyr BP and the transition from the LGM to preindustrial, showing some deficit in the second half of T1 and in the Holocene (Fig. 5b). The PGM-to-LGM trend of $0.45\%_0$ and the minimum around

60 kyr BP are both largely unexplained in this simulation. The attribution of changes in $\delta^{13}CO_2$ to individual processes in the ocean and land carbon cycle has been done before for the precursor model BICYCLE (Köhler et al., 2005, 2010) and is not repeated here, since the misfit to the data indicates some fundamental shortcomings.

The way in which simulated changes in atmospheric $\delta^{13}CO_2$ compare to simulated changes in various marine $\delta^{13}C_{DIC}$ time series is shown for scenario SEi in Fig. 7a, b. Both global mean surface $\delta^{13}C_{DIC}$ and wider tropical surface $\delta^{13}C_{DIC}$ show clear similarities with atmospheric $\delta^{13}CO_2$. Here, surface values are area-weighted averages covering either the global ocean or the two equatorial ocean boxes in the case of the wider tropics, which spatially cover a similar area to the sediment cores used for our new stacks, $\Delta(\delta^{13}C_{rub})$ and $\Delta(\delta^{13}C_{sac})$. During glacial times and the onset of deglaciations, the dynamics in the global mean surface $\delta^{13}C_{DIC}$ (cyan line in Fig. 7a) are in close agreement with $\delta^{13}CO_2$ in the atmosphere (broken black line in Fig. 7a), while for the later part of the deglaciations and the interglacials the dynamics in the wider tropical surface $\delta^{13}C_{DIC}$ (magenta line in Fig. 7a) fit better to $\delta^{13}CO_2$ in the atmosphere. This difference is probably explained by the dynamics in the polar oceans. During glacial times, the Southern Ocean is highly stratified with little vertical exchange between the surface ocean and the deep ocean. This stratification breaks down during the terminations and in the interglacials, allowing a faster exchange of tracers between the surface ocean and the deep ocean, leading to smaller surface-to-deep gradients in $\delta^{13}C_{DIC}$ in the polar oceans. In other words, the lower deep-ocean $\delta^{13}C_{DIC}$ values have a larger impact on polar surface $\delta^{13}C_{DIC}$ during interglacials than during glacials, leading to a divergence in $\delta^{13}C_{DIC}$ in the global mean surface and in the wider tropical surface ocean. The scatter plots between atmospheric $\delta^{13}CO_2$ and either global mean surface or wider tropical surface-ocean $\delta^{13}C_{DIC}$ show that the latter has the higher correlation (Fig. S2; $r^2 = 0.82$ vs. $r^2 = 0.59$). Furthermore, frequency analysis showed that the coherence between atmospheric $\delta^{13}CO_2$ and wider tropical surface-ocean $\delta^{13}C_{DIC}$ is in periodicities slower than 20 kyr higher than between atmospheric $\delta^{13}CO_2$ and global mean surface-ocean $\delta^{13}C_{DIC}$ (Fig. S3a). This implies that simulations which agree in atmospheric $\delta^{13}CO_2$ with reconstructions (which will be achieved later on in scenarios C1 and C1CO2) should contain a very likely realisation of $\delta^{13}C_{DIC}$ in the wider tropical surface ocean. A comparison of these simulated time series with our new mono-specific $\delta^{13}C$ stacks should therefore enable us to address if and how $\delta^{13}C$ has been modified during hard-shell formation. For scenario SEi the misfit in simulated wider tropical surface-ocean $\delta^{13}C_{DIC}$ and the new $\delta^{13}C$ reconstructions (Fig. 7a) is large, but it is as yet unclear if this discrepancy can be explained by the CIE or by other processes.

To understand how representative the reconstructed $\delta^{13}C$ stack from benthic foraminifera in six deep Pacific cores
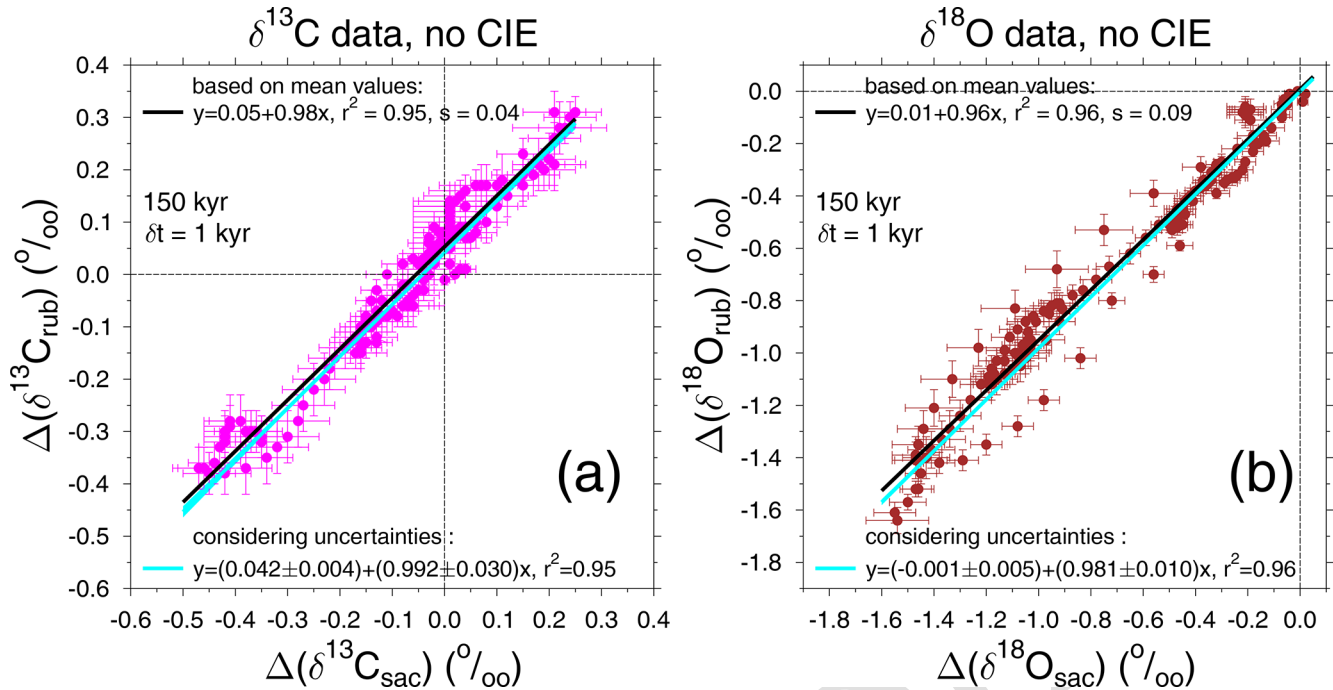
Figure 6. Scatter plot of our new stacks, **(a)** $\Delta(\delta^{13}C_{rub})$ versus $\Delta(\delta^{13}C_{sac})$ and **(b)** $\Delta(\delta^{18}O_{rub})$ versus $\Delta(\delta^{18}O_{sac})$. Data stacks without corrections for the CIE are plotted. The time series are restricted to data from the last 150 kyr to allow a comparison later on with simulation results, which were based on the only 155 kyr long atmospheric $\delta^{13}CO_2$ record. Linear regressions using only the mean values and also when using uncertainties in both x and y are performed. The root-mean-square error is depicted by s.

(Lisiecki, 2014) might be, we compare it with various different simulated time series: $\delta^{13}C_{DIC}$ in the deep Indo-Pacific, in the mean deep ocean and in the mean ocean (Fig. 7b). Here, deep-ocean results from the model refer to ocean boxes that contain waters deeper than 1 km. As expected, the deep Indo-Pacific contains the end member of the $\delta^{13}C$ cycle with the most depleted values. The mean deep-ocean $\delta^{13}C_{DIC}$ is offset by 0.2‰–0.4‰ towards more positive values and shows larger G-IG amplitudes than $\delta^{13}C_{DIC}$ does in the deep Indo-Pacific. The mean ocean is again 0.2‰–0.4‰ more positive in $\delta^{13}C_{DIC}$ than the mean deep ocean, again with smaller G-IG amplitudes of 0.53‰ across T1. This number compares $\delta^{13}C_{DIC}$ in the last 6 kyr with the mean at the LGM (23–19 kyr BP), similarly as in Peterson et al. (2014), who proposed a mean ocean rise in $\delta^{13}C$ by 0.34 ± 0.19‰. However, be aware that in Peterson et al. (2014) the CIE in benthic foraminifera as deduced in Schmittner et al. (2017) is not included. This suggests that the reconstructions are potentially recording a smaller G-IG change in $\delta^{13}C$ than how $\delta^{13}C_{DIC}$ in the deep ocean might have changed.

When discussing the results of scenario SEi (Fig. 7a), we have shown that, once changes in the atmospheric $\delta^{13}CO_2$ are met by the simulations, the model should then also give a reasonable answer for what $\delta^{13}C_{DIC}$ in the wider tropical surface ocean might have looked like. Furthermore, the close agreement in simulated and reconstructed atmospheric CO_2 (Fig. 5a) suggests that the assumed carbon cycle changes in

our approach might be one possible realisation that is not too far away from the real-world changes. However, the misfit between simulation results from scenario SEi and reconstruction in the $\delta^{13}C$ cycle, where linear regressions between simulations and reconstructions found no correlation at all ($r^2 \leq 0.02$; Fig. S4a, b), is not easily fixed. To improve our results, we force the model with the atmospheric records (scenario C1 only using $\delta^{13}CO_2$ and scenario C1CO2 using both $\delta^{13}CO_2$ and CO_2) to have conditions in the surface ocean as close to reconstructions as possible. Doing so leads to even tighter correlations between simulated atmospheric $\delta^{13}CO_2$ and simulated $\delta^{13}C_{DIC}$ in the surface ocean than what we obtained for scenario SEi: the r^2 correlations between these variables are in scenarios C1 and C1CO2, with prescribed atmospheric $\delta^{13}CO_2 \geq 0.77$ and ≥ 0.88 for global mean surface $\delta^{13}C_{DIC}$ and wider tropical surface $\delta^{13}C_{DIC}$, respectively (Fig. S2). Again, the coherence is higher between atmospheric $\delta^{13}CO_2$ and the wider tropical surface-ocean $\delta^{13}C_{DIC}$ than between atmospheric $\delta^{13}CO_2$ and the global mean surface-ocean $\delta^{13}C_{DIC}$ (Fig. S3b). Furthermore, in both scenarios, the changes in simulated $\delta^{13}C_{DIC}$ in the wider tropical surface ocean agree remarkably well (r^2 between 0.76 and 0.78; Fig. S4c–f) with changes in our new stacks $\Delta(\delta^{13}C_{rub})$ and $\Delta(\delta^{13}C_{sac})$ without consideration of the CIE (Fig. 7c), at least on orbital timescales. This effect is also seen by the rise in coherence between simulated wider tropical surface $\delta^{13}C_{DIC}$ and both our stacks from less than
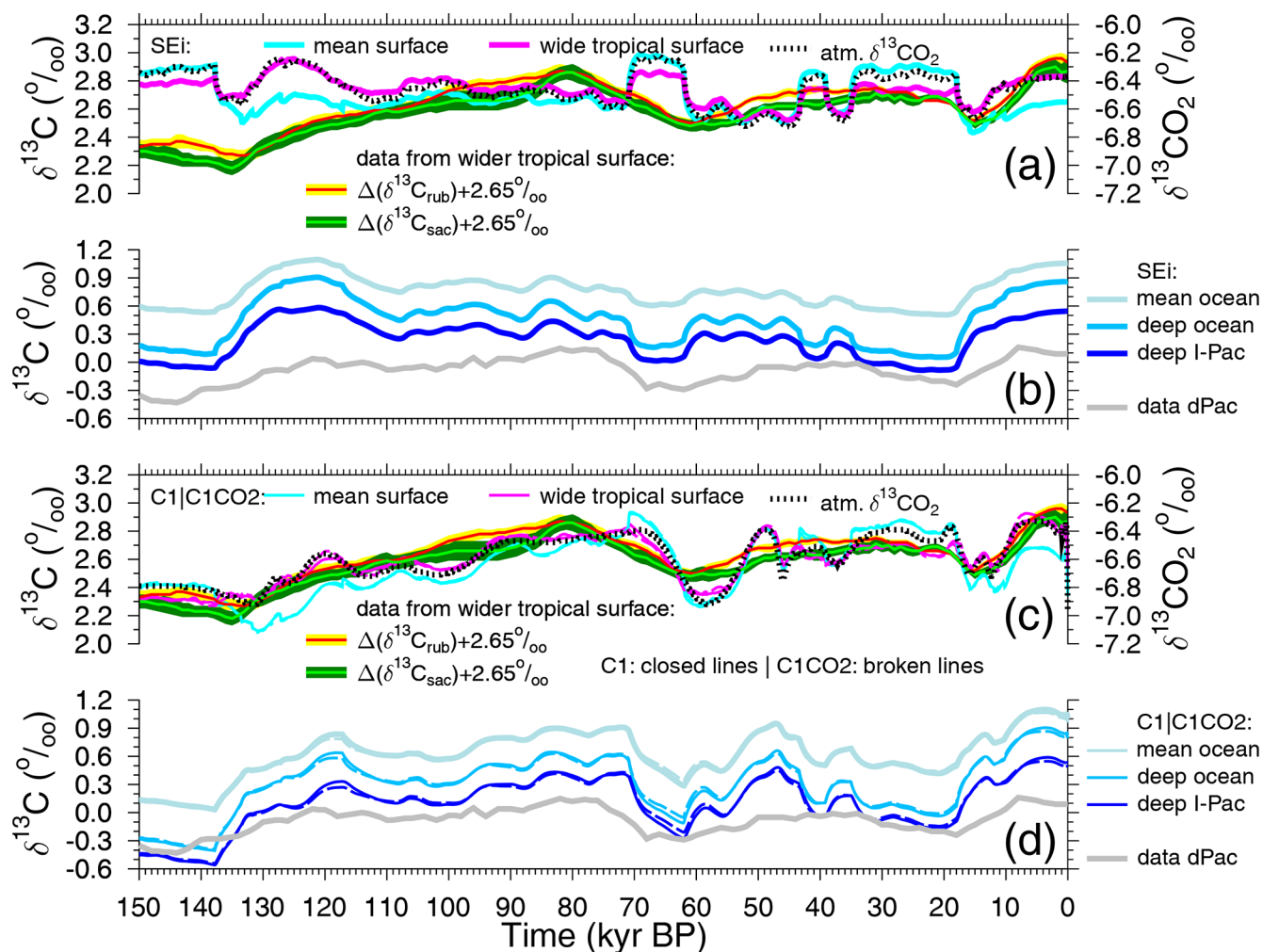
Figure 7. Simulated surface- and deeper-ocean δ^{13}C time series from scenario SEi **(a, b)** and scenarios C1 and C1CO2 **(c, d)** compared with reconstructions. **(a, c)** Simulated δ^{13}C$_{DIC}$ in the global mean surface ocean and in the wider tropical surface ocean together with simulated atmospheric δ^{13}CO$_2$ (right y axis) are plotted together with our new stacks from the wider tropical surface ocean, with $\Delta(\delta^{13}$C$_{rub})$ and $\Delta(\delta^{13}$C$_{sac})$ shifted by $+2.65$‰ to meet simulated surface δ^{13}C$_{DIC}$ at the LGM. In panels **(b)** and **(d)**, simulated δ^{13}C$_{DIC}$ for the deep Indo-Pacific (I-Pac), the mean deep ocean and the mean global ocean are plotted together with δ^{13}C from benthic foraminifera stacked from six cores in the deep Pacific (dPac) (Lisiecki, 2014). In panels **(c)** and **(d)**, the scenarios C1 (closed lines) and C1CO2 (broken lines) are plotted together. Most of the time the differences between both are so small that the lines are indistinguishable.

0.1 (scenario SEi) to higher than 0.7 (scenario C1CO2) in the 41 and 100 kyr bands (Fig. S3c, d), while in the precession bands (19 and 23 kyr) the coherence stayed below 0.6. Some more abrupt changes contained in the simulations are not recorded in the reconstructions, probably because bioturbation in the surface sediments, together with the stacking procedure, prevent our marine records from successfully resolving millennial-scale features. Thus, our forcing of atmospheric carbon records with data therefore seems to be a promising approach to obtain simulated surface ocean in agreement with reconstructions for the slow-frequency bands (41 kyr and beyond), while it seems to fail for precession and faster changes. When forcing atmospheric δ^{13}CO$_2$ by data, the temperature-dependent isotopic fractionation dur-

ing marine photosynthesis in $\varepsilon_{(C_{org}-DIC)}$ is only of minor importance for the simulated surface-ocean δ^{13}C$_{DIC}$. If this effect is switched off, the δ^{13}C$_{DIC}$ in the wider tropical surface ocean differs in general by less than 0.05‰ from the values in scenario C1.

Furthermore, deep-ocean δ^{13}C$_{DIC}$ is now, on an orbital timescale, also in better agreement with the data (Fig. 7d), the r^2 of a linear regression between simulated deep Indo-Pacific δ^{13}C$_{DIC}$, and the reconstructed deep Pacific rises from 0.49 for scenario SEi to 0.77 and above for the scenarios forced by atmospheric carbon records (Fig. S5), although the rise in mean ocean δ^{13}C$_{DIC}$ during T1 has now been increased to 0.59‰. Considering a CIE of -2.6×10^{-3}‰ per µmol kg^{-1} of [CO$_3^{2-}$] disturbance for epibenthic foraminifera (Schmit-

tner et al., 2017), simulated variations in deep-ocean $[CO_3^{2-}]$ of $+20\,\mu mol\,kg^{-1}$ (Köhler and Munhoven, 2020) would translate to a comparably small reduction in deep Pacific benthic $\delta^{13}C$ of up to $0.05\%o$. While the timing of changes in deep-ocean $[CO_3^{2-}]$ with highest values during the deglaciation is crucial to assess how such a benthic CIE would reduce the existing data–model mismatch, a more thorough assessment of the benthic CIE would require the comprehensive compilation of benthic $\delta^{13}C$ time series in different ocean basins, which is beyond the scope of this study. Note that the approximated amplitude of this benthic CIE is close to the measurement error of benthic $\delta^{13}C$.

3.3 The importance of the carbonate ion effect for wider tropical surface-ocean $\delta^{13}C$

Although the initial analysis of our results when forced with atmospheric records already suggests only a minor, if any, role for the CIE in the interpretation of stacked mono-specific $\delta^{13}C$ on orbital timescales, in the following section we make a more quantitative assessment. The CIE has not yet been implemented in the ^{13}C cycle of the model, but it is only investigated here in post-processing. The carbonate ion concentration of either global mean surface waters or wider tropical mean surface waters in our simulations is tightly anti-correlated with atmospheric CO_2 ($r^2 \geq 0.93$; Fig. S6), which is a consequence of the marine carbonate system (Zeebe and Wolf-Gladrow, 2001). Both scenarios C1 and C1CO2 lead to rather similar results here, which suggests that the CO_2 forcing in scenario C1CO2 and its violation of mass conservation are perturbing the carbon cycle only slightly. To stay as closely as possible to the reconstructions, we nevertheless continue in the following section by using results from scenario C1CO2, but results differ only slightly when based in scenario C1; thus our conclusions are independent from this choice.

Thus, CO_3^{2-} in the wider tropical surface ocean in the simulation typically falls from maximum glacial values of $\sim 320\,\mu mol\,kg^{-1}$ to interglacial minima of $\sim 250\,\mu mol\,kg^{-1}$ across both Terminations 1 and 2 (Fig. 8a). This translates into a potential CIE of about $0.62\%o$ (Fig. 8b) for *G. ruber* when we use the slope of $m = -0.0089\%o$ per $\mu mol\,kg^{-1}$ change in $[CO_3^{2-}]$ and of $0.33\%o$ for *T. sacculifer* (slope of $m = -0.0047\%o$ per $\mu mol\,kg^{-1}$ change in $[CO_3^{2-}]$) (Spero et al., 1999). The y axis intercepts of the complete regressions for the CIE is determined in order to have a maximum agreement between reconstructions and simulations during the LGM. When comparing the potential CIE to the simulated LGM-to-preindustrial (PRE) amplitude of only $0.16\%o$ in wider tropical surface waters (Fig. 8c), the CIE-to-G-IG ratios are between a factor of 2 and 4, and CIE signals should clearly stand out in the paleo-records. If we add this CIE to our simulated mean equatorial surface-ocean $\delta^{13}C_{DIC}$ (Fig. 8c), we end up with time series, which should compare well with the mono-species stacks of $\Delta(\delta^{13}C_{rub})$ and

$\Delta(\delta^{13}C_{sac})$ (Fig. 8d). However, this is not the case. The r^2 in the linear regressions between CIE-corrected $\delta^{13}C_{DIC}$ in wider tropical surface waters and reconstructions is reduced to 0.54 (*G. ruber*) and 0.68 (*T. sacculifer*), while it had been ≥ 0.76 without CIE correction (Figs. S4, S7). When plotting results as hypothetically recorded in both species against each other, we obtain a slope of 1.26 (Fig. S8a). The slope between the stacked mono-specific $\delta^{13}C$ time series without further correction for a CIE was ~ 0.99 (Fig. 6a). The consideration of the CIE did not lead to time series which agree better with each other. Thus, we conclude that both species, *G. ruber* and *T. sacculifer*, are already good recorders of changes in $\delta^{13}C_{DIC}$ in wider tropical surface-ocean waters on orbital timescales.

3.4 Carbonate ion effect in $\delta^{18}O$

The focus of this study is on stable carbon isotope $\delta^{13}C$. However, during the construction of our mono-specific wider tropical stacks of $\Delta(\delta^{13}C_{rub})$ and $\Delta(\delta^{13}C_{sac})$, the corresponding stacks of $\Delta(\delta^{18}O_{rub})$ and $\Delta(\delta^{18}O_{sac})$ are easily generated by-products initially used to cross-check the applied age models. However, these $\delta^{18}O$ data give us the possibility to also have a closer look at the role of the CIE in the recording of oxygen isotopes in foraminiferal shells. For that endeavour, we need a background time series of $\delta^{18}O$ which represents the signals when not modified by the CIE. Such a mean $\delta^{18}O$ in the wider tropical surface ocean should record the same sea-level-related variations as the average global ocean, but it might differ in the recorded temperature effect if the change in the average wider tropical sea surface temperature differed from the mean ocean temperature (MOT) change. Pöppelmeier et al. (2023) showed that the LGM-to-PRE change in the MOT derived from the model-based interpretation of noble gas reconstructions in ice cores is $2.1 \pm 0.7\,K$. The reconstructed rise in the MOT is slightly higher when ignoring the effect of past saturation changes on noble gases (Shackleton et al., 2023). The data assimilation effort in LGM temperature changes by Tierney et al. (2020) is broadly in agreement with the MOT change of Pöppelmeier et al. (2023) and proposes that the tropical ($30°$ S to $30°$ N) sea surface was around $2.6\,K$ colder at the LGM than at the PRE, agreeing within the uncertainties with the MOT change. To a first order, we therefore assume that the planktic foraminifera should record the same temperature effect in $\delta^{18}O$ as contained in the mean ocean. Thus, the global ocean $\delta^{18}O$ calculated from stacking benthic time series (Lisiecki and Stern, 2016) represents the CIE-free background against which we compare our new $\Delta(\delta^{18}O_{rub})$ and $\Delta(\delta^{18}O_{sac})$ stacks.

From the simulated LGM-to-PRE change in mean wider tropical surface-ocean CO_3^{2-} of about $-70\,\mu mol\,kg^{-1}$ (Fig. 8e) and the laboratory-based amplitudes of the CIE ($-0.0022\%o$ and $-0.0014\%o$ change in $\delta^{18}O$ per $\mu mol\,kg^{-1}$ for *G. ruber* and *T. sacculifer*, respectively (Spero et al.,
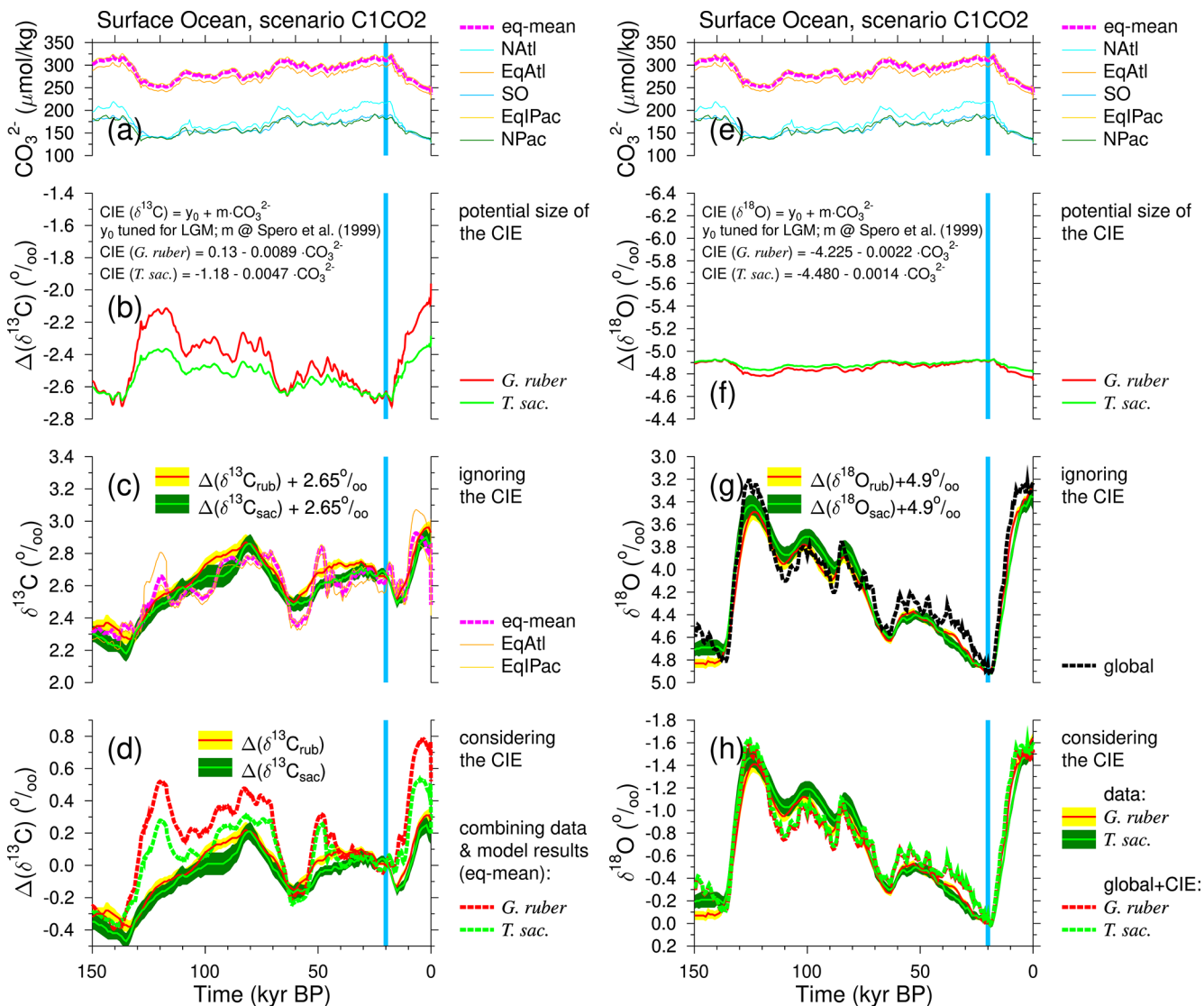
Figure 8. Calculating the suggested carbonate ion effects (CIE) on *G. ruber* and *T. sacculifer*. The left-hand column shows the effects on δ^{13}C, while the right column shows the effects on δ^{18}O. **(a, e)** Surface-ocean [CO_3^{2-}]. **(b, f)** Potential CIE using slopes from Spero et al. (1999). **(c, g)** Surface-ocean conditions when ignoring the CIE or **(d, h)** when considering the CIE. Mean anomalies (± 1 SE) of the isotope stacks are calculated with respect to the mean of 21–19 kyr BP (vertical blue band). Simulations use the results from scenario C1CO2. Different surface-ocean areas are distinguished: North Atlantic (NAtl; north of 50° N), equatorial Atlantic (EqAtl; 40° S–50° N), Southern Ocean (SO; south of 40° S), equatorial Indo-Pacific (EqIPac; 40° S–40° N) and North Pacific (NPac; north of 40° N). The mean wider tropical ocean in the model is the mean from the equatorial boxes (eq-mean).

1999)), we determined that $\Delta(\delta^{18}O_{rub})$ and $\Delta(\delta^{18}O_{sac})$ should record the changes since the LGM by $+0.15\,$‰ and $+0.10\,$‰ differently than how δ^{18}O in the surface waters truly changed (Fig. 8f). Compared to the G-IG amplitude in mean ocean δ^{18}O of $-1.65\,$‰ (Fig. 8g), these potential CIEs represent corrections of $-9\,\%$ and $-6\,\%$, a difference of 3 % which might be difficult to detect in the paleo-records. A linear regression through a scatter plot of $\delta^{18}O + CIE_{rub}$ versus $\delta^{18}O + CIE_{sac}$ has a slope of 0.97 ($r^2 = 1.00$; Fig. S8b), which is indistinguishable from the slope obtained from re-

gression through the data stacks (Fig. 6b), while the slope when considering the CIE should move to unity (indicating that both species were recording the same signal underneath the CIE) if the effect plays an important role during data interpretation. The evidence for or against the CIE in δ^{18}O from both data and models is therefore inconclusive.

4   Conclusions

The CIE for δ^{13}C and δ^{18}O recorded in planktic foraminifera was first identified in laboratory experiments (Spero et al., 1997, 1999), and it was, based on theory, suggested for both isotopes that the underlying processes are directly related to the pH in the surrounding seawater during hard-shell formation (Zeebe et al., 1999; Zeebe, 1999). However, these theoretical studies were already unable to confirm the full range of the CIE as contained in the experiments. Furthermore, according to Bijma et al. (1999), it is impossible to determine if pH or $[CO_3^{2-}]$ is responsible for the observed fractionation effects. If this theoretical understanding is correct, we would expect to see the CIE in neither or both isotopes in the our mono-specific stacks. Thus, although the interpretation of δ^{18}O with respect to the CIE is uncertain due to the signal-to-noise ratio, we argue, based on the clear evidence of a lack of the CIE in the recording of δ^{13}C in *G. ruber* and *T. sacculifer*, that there is probably also no significant CIE contained in the δ^{18}O time series of both species. This finding argues against the suggestion of Spero et al. (1999) that the CIE and δ^{13}C time series from *G. ruber* and *T. sacculifer* might be used to calculate a record of surface-ocean $[CO_3^{2-}]$. Furthermore, we suggest using our new stack of $\Delta(\delta^{13}C_{\mathrm{rub}})$ as representative of $\delta^{13}C_{\mathrm{DIC}}$ in the wider tropical surface ocean.

Various possible explanations for the lack of a CIE on orbital timescales exist. Firstly, it might be that the isotopic fractionation during hard-shell formation in *G. ruber* and *T. sacculifer* is rather insensitive to $[CO_3^{2-}]$ in the range of interest (250–320 μmol kg^{-1}). Such an insensitivity has been suggested for other species (Bijma et al., 1999), but, due to a lack of published data (the slopes of the CIE in *G. ruber* and *T. sacculifer* were only summarised in Spero et al. (1999), while underlying experiments have never been published in the peer-reviewed literature), it cannot be properly checked for the two species investigated here. Secondly, not the CIE, but alternatively the incorporation of respired CO_2 (depleted in δ^{13}C) during shell formation, might be responsible for the observed isotope data in laboratory experiments performed with *Orbulina universa* and *Globigerina bulloides* (Bijma et al., 1999). This process might also play a role in *G. ruber* and *T. sacculifer*, but it would only explain observed effects in δ^{13}C and not in δ^{18}O. However, since our stacks are inconclusive with respect to the CIE and δ^{18}O, they might be of relevance here. A third explanation might be related to homeostasis. In symbiont-bearing planktic foraminifera, such as *G. ruber* and *T. sacculifer*, the pH at the shell surface critically depends on photosynthesis and hence light levels and symbiont density (Jørgensen et al., 1985). In order to facilitate calcification, *G. ruber* and *T. sacculifer* may actively influence the pH at the shell surface by seeking specific (optimum) light levels through vertical migration, thereby keeping the CIE constant over time. Planktic foraminifera are known to move vertically in the water column (e.g. Kimoto, 2015). Vertical migration to optimise both nutrient uptake

and light has been proposed to play an important role in phytoplankton by modelling (Wirtz et al., 2022), an effect which has recently been supported by field data (Zheng et al., 2023). We speculate that similar behaviour could occur in the two planktic foraminifera species. Indeed, Jonkers and Kučera (2017) and Daëron and Gray (2023) found that δ^{18}O in various planktic foraminifera (including *G. ruber* and *T. sacculifer*) is best explained by also considering calcification in waters deeper than their expected living depth.

It is too early to be able to generalise our finding that on orbital timescales the CIE plays no role in the interpretation of signals in planktic foraminifera in paleo-records. For that endeavour, more mono-specific stacks are necessary, preferably from conceptually different foraminifera species without symbionts or spines, as these might potentially show a different behaviour with respect to light (and pH) optimisation. However, our findings might suggest that previous studies on planktic δ^{13}C, which ignored the CIE (e.g. Lynch-Stieglitz et al., 2019; Lund et al., 2019), might not be biased.

Our carbon cycle simulations confirm that atmospheric $\delta^{13}CO_2$ and mean surface-ocean $\delta^{13}C_{\mathrm{DIC}}$ are tightly related to each other, highlighting the importance of air–sea gas exchange for carbon isotopes. This is not entirely new, and it has already been discussed before (e.g. Lynch-Stieglitz et al., 2019; Shao et al., 2021; Pinho et al., 2023). However, the ^{13}C cycle is more complex than stated previously (Lynch-Stieglitz et al., 2019; Hu et al., 2020; Pinho et al., 2023). These studies suggested that one might calculate a mean surface-ocean $\delta^{13}C_{\mathrm{DIC}}$ as a function of atmospheric $\delta^{13}CO_2$ and a temperature-dependent fractionation during gas exchange. We assumed here, based on modern data from Verwega et al. (2021), that species composition, and therefore isotopic fractionation during marine photosynthesis, might also be temperature-dependent, having an important impact on surface-ocean $\delta^{13}C_{\mathrm{DIC}}$. Furthermore, our simulation results show that $\delta^{13}C_{\mathrm{DIC}}$ in polar oceans and in the wider tropical surface ocean have a different and time-dependent relation to atmospheric $\delta^{13}CO_2$.

Finally, since our simulations were forced by atmospheric carbon records, we are unable to identify specific processes being responsible for the simulated changes in the ^{13}C cycle. Recent climate simulations (Yun et al., 2023) emphasise the importance of the 405 kyr eccentricity cycle in tropical hydroclimate. It therefore seems reasonable that the missing long-term variability in δ^{13}C in our setup might indeed be connected to weathering fluxes, as proposed before (e.g. Schneider et al., 2013; Wang et al., 2014), something which needs to be tested in more detail in future carbon cycle simulation studies.

Code and data availability. PaleoDataView was used for planktic data processing (Langner and Mulitza, 2019). In Table S1, metadata on the data selection are contained, including references to the original publications. The reference list based on citations in the Supplement (Table S1) is separately attached to the end of the main text. Most of the data from the planktic foraminifera *G. ruber* and *T. sacculifer* are already contained in the World Atlas of late Quaternary Foraminiferal Oxygen and Carbon Isotope Ratios (https://doi.org/10.1594/PANGAEA.936747; Mulitza et al., 2021; Mulitza et al., 2022). The data sets not yet contained in the World Atlas can be found at https://doi.org/10.1594/PANGAEA.726202 (Duplessy, 1982; https://www.ncei.noaa.gov/pub/data/paleo/paleocean/climap/climap18/; CLIMAP Project Members, 1994) and at https://doi.org/10.1594/PANGAEA.54765 (Meinecke, 1999) and in three theses (Zahn-Knoll, 1986; Slowey, 1990; Romahn, 2014), from which data have been manually extracted from Tables. Simulation results and the data contributing to our data compilation including raw data, the BACON settings and a netCDF file of the PaleoDataView Collection, are available at PANGAEA (https://doi.org/10.1594/PANGAEA.963761, Köhler and Mulitza, 2023). Data for atmospheric CO_2 and $\delta^{13}CO_2$ are found in Eggleston et al. (2016b) (https://doi.org/10.1594/PANGAEA.859181), Köhler et al. (2017b) (https://doi.org/10.1594/PANGAEA.871273) and Menking et al. (2022a) (https://doi.org/10.15784/601600). The stack of deep Pacific benthic $\delta^{13}C$ is contained in Köhler (2022) (https://doi.org/10.1594/PANGAEA.940169).

Supplement. The supplement related to this article is available online at: https://doi.org/10.5194/cp-20-1-2024-supplement.

Author contributions. PK designed the study, performed the simulations, analysed the data and led the writing of the draft. SM generated the age models and the planktic time series and contributed to the writing of the draft.

Competing interests. The contact author has declared that neither of the authors has any competing interests.

Disclaimer. Publisher's note: Copernicus Publications remains neutral with regard to jurisdictional claims made in the text, published maps, institutional affiliations, or any other geographical representation in this paper. While Copernicus Publications makes every effort to include appropriate place names, the final responsibility lies with the authors.

Acknowledgements. This work is supported by the German Federal Ministry of Education and Research (BMBF) as a Research for Sustainability initiative (FONA; https://www.fona.de/de/, last access: 18 April 2024) through the PalMod project. We thank Peter U. Clark for providing the SST data connected to Barth et al. (2018) and Jelle Bijma for discussions.

Financial support. This research has been supported by the Bundesministerium für Bildung und Forschung (grant no. 01LP1922A).

The article processing charges for this open-access publication were covered by the Alfred-Wegener-Institut Helmholtz-Zentrum für Polar- und Meeresforschung.

Review statement. This paper was edited by Luc Beaufort and reviewed by Andreas Schmittner and one anonymous referee.

References

Al-Rousan, S., Pätzold, J., Al-Moghrabi, S., and Wefer, G.: Invasion of anthropogenic CO_2 recorded in planktonic foraminifera from the northern Gulf of Aqaba, Int. J. Earth Sci., 93, 1066–1076, https://doi.org/10.1007/s00531-004-0433-4, 2004.

Bachan, A., Lau, K. V., Saltzman, M. R., Thomas, E., Kump, L. R., and Payne, J. L.: A model for the decrease in amplitude of carbon isotope excursions across the Phanerozoic, Am. J. Sci., 317, 641–676, https://doi.org/10.2475/06.2017.01, 2017.

Barth, A. M., Clark, P. U., Bill, N. S., He, F., and Pisias, N. G.: Climate evolution across the Mid-Brunhes Transition, Clim. Past, 14, 2071–2087, https://doi.org/10.5194/cp-14-2071-2018, 2018.

Bauska, T. K., Baggenstos, D., Brook, E. J., Mix, A. C., Marcott, S. A., Petrenko, V. V., Schaefer, H., Severinghaus, J. P., and Lee, J. E.: Carbon isotopes characterize rapid changes in atmospheric carbon dioxide during the last deglaciation, P. Natl. Acad. Sci. USA, 113, 3465–3470, https://doi.org/10.1073/pnas.1513868113, 2016.

Bauska, T. K., Brook, E. J., Marcott, S. A., Baggenstos, D., Shackleton, S., Severinghaus, J. P., and Petrenko, V. V.: Controls on Millennial-Scale Atmospheric CO_2 Variability During the Last Glacial Period, Geophys. Res. Lett., 45, 7731–7740, https://doi.org/10.1029/2018GL077881, 2018.

Bereiter, B., Eggleston, S., Schmitt, J., Nehrbass-Ahles, C., Stocker, T. F., Fischer, H., Kipfstuhl, S., and Chappellaz, J.: Revision of the EPICA Dome C CO_2 record from 800 to 600 kyr before present, Geophys. Res. Lett., 42, 542–549, https://doi.org/10.1002/2014GL061957, 2015.

Bijma, J., Spero, H. J., and Lea, D. W.: Reassessing Foraminiferal Stable Isotope Geochemistry: Impact of the Oceanic Carbonate System (Experimental Results), Springer Berlin Heidelberg, Berlin, Heidelberg, 489–512, https://doi.org/10.1007/978-3-642-58646-0_20, 1999.

Blaauw, M. and Christen, J. A.: Flexible paleoclimate age-depth models using an autoregressive gamma process, Bayesian Anal., 6, 457–474, https://doi.org/10.1214/11-BA618, 2011.

Black, D., Thunell, R., Wejnert, K., and Astor, Y.: Carbon isotope composition of Caribbean Sea surface waters: Response to the uptake of anthropogenic CO_2, Geophys. Res. Lett., 38, L16609, https://doi.org/10.1029/2011GL048538, 2011.

Brandenburg, K. M., Rost, B., Van de Waal, D. B., Hoins, M., and Sluijs, A.: Physiological control on carbon isotope fractionation in marine phytoplankton, Biogeosciences, 19, 3305–3315, https://doi.org/10.5194/bg-19-3305-2022, 2022.

Browaeys, J.: Linear fit with both uncertainties in x and in y, MATLAB Central File Exchange, [code],

https://www.mathworks.com/matlabcentral/fileexchange/
45711-linear-fit-with-both-uncertainties-in-x-and-in-y   (last
access: 16 October 2023), 2023.

Buitenhuis, E. T., Le Quéré, C., Bednaršek, N., and
Schiebel, R.: Large Contribution of Pteropods to Shallow
CaCO$_3$ Export, Global Biogeochem. Cy., 33, 458–468,
https://doi.org/10.1029/2018GB006110, 2019.

Butzin, M., Heaton, T. J., Köhler, P., and Lohmann, G.: A short note
on marine reservoir age simulations used in IntCal20, Radiocar-
bon, 62, 865–871, https://doi.org/10.1017/RDC.2020.9, 2020.

CLIMAP Project Members: CLIMAP 18K Database, IGBP
PAGES/World Data Center-A for Paleoclimatology Data Con-
tribution Series # 94-001, NOAA/NGDC Paleoclimatology
Program, Boulder CO, USA, https://www.ncei.noaa.gov/pub/
data/paleo/paleocean/climap/climap18/ (last access: 16 Novem-
ber 2023), 1994.

Curry, W. B. and Crowley, T. J.: The δ^{13}C of equatorial Atlantic sur-
face waters: implications for ice age pCO$_2$ levels, Paleoceanog-
raphy, 2, 489–517, https://doi.org/10.1029/PA002i005p00489,
1987.

Daëron, M. and Gray, W. R.: Revisiting Oxygen-18 and
Clumped Isotopes in Planktic and Benthic Foraminifera, Pa-
leoceanography and Paleoclimatology, 38, e2023PA004660,
https://doi.org/10.1029/2023PA004660, 2023.

Deines, P.: The carbon isotope geochemistry of mantle xenoliths,
Earth-Sci. Rev., 58, 247–278, https://doi.org/10.1016/S0012-
8252(02)00064-8, 2002.

Duplessy, J.-C.: (Table 2) Stable carbon and oxygen isotope ratios
of Globigerinoides ruber from sediment core MD77-169, PAN-
GAEA [data set], https://doi.org/10.1594/PANGAEA.726202,
1982.

Eggleston, S., Schmitt, J., Bereiter, B., Schneider, R., and Fischer,
H.: Evolution of the stable carbon isotope composition of atmo-
spheric CO$_2$ over the last glacial cycle, Paleoceanography, 31,
434–452, https://doi.org/10.1002/2015PA002874, 2016a.

Eggleston, S., Schmitt, J., Bereiter, B., Schneider, R., and
Fischer, H.: CO$_2$ concentration and stable isotope ra-
tios of three Antarctic ice cores covering the period
from 149.4–1.5 kyr before 1950, PANGAEA [data set],
https://doi.org/10.1594/PANGAEA.859181, 2016b.

Eide, M., Olsen, A., Ninnemann, U. S., and Eldevik, T.: A
global estimate of the full oceanic ^{13}C Suess effect since
the preindustrial, Global Biogeochem. Cy., 31, 515–534,
https://doi.org/10.1002/2016GB005472, 2017.

Emiliani, C.: Pleistocene temperatures, J. Geol., 63, 539–578, 1955.

Felis, T., Hinestrosa, G., Köhler, P., and Webster, J. M.: Role
of the deglacial buildup of the Great Barrier Reef for the
global carbon cycle, Geophys. Res. Lett., 49, e2021GL096495,
https://doi.org/10.1029/2021GL096495, 2022.

Fraile, I., Schulz, M., Mulitza, S., and Kucera, M.: Predict-
ing the global distribution of planktonic foraminifera using
a dynamic ecosystem model, Biogeosciences, 5, 891–911,
https://doi.org/10.5194/bg-5-891-2008, 2008.

Ganopolski, A. and Brovkin, V.: Simulation of climate, ice sheets
and CO$_2$ evolution during the last four glacial cycles with an
Earth system model of intermediate complexity, Clim. Past, 13,
1695–1716, https://doi.org/10.5194/cp-13-1695-2017, 2017.

Hauck, J., Zeising, M., Le Quéré, C., Gruber, N., Bakker, D. C. E.,
Bopp, L., Chau, T. T. T., Gürses, Ö., Ilyina, T., Landschützer,

P., Lenton, A., Resplandy, L., Rödenbeck, C., Schwinger, J., and
Séférian, R.: Consistency and Challenges in the Ocean Carbon
Sink Estimate for the Global Carbon Budget, Front. Mar. Sci., 7,
852, https://doi.org/10.3389/fmars.2020.571720, 2020.

Heaton, T. J., Köhler, P., Butzin, M., Bard, E., Reimer, R. W.,
Austin, W. E., Ramsey, C. B., Grootes, P. M., Hughen,
K. A., Kromer, B., Reimer, P. J., Adkins, J. F., Burke,
A., Cook, M. S., Olsen, J., and Skinner, L. C.: Ma-
rine20 – the marine radiocarbon age calibration curve (0–
55,000 cal BP), simulated data for IntCal20, PANGAEA [data
set], https://doi.org/10.1594/PANGAEA.914500, 2020a.

Heaton, T. J., Köhler, P., Butzin, M., Bard, E., Reimer, R. W.,
Austin, W. E. N., Ramsey, C. B., Grootes, P. M., Hughen, K. A.,
Kromer, B., Reimer, P. J., Adkins, J., Burke, A., Cook, M. S.,
Olsen, J., and Skinner, L. C.: Marine20 – the marine radiocar-
bon age calibration curve (0–55,000 cal BP), Radiocarbon, 62,
779–820, https://doi.org/10.1017/RDC.2020.68, 2020b.

Hu, R., Bostock, H. C., Greaves, M., Piotrowski, A. M.,
and McCave, I. N.: Coupled evolution of stable carbon
isotopes between the Southern Ocean and the atmosphere
over the last 260 ka, Earth Planet. Sc. Lett., 538, 116215,
https://doi.org/10.1016/j.epsl.2020.116215, 2020.

Jonkers, L. and Kučera, M.: Quantifying the effect of seasonal
and vertical habitat tracking on planktonic foraminifera prox-
ies, Clim. Past, 13, 573–586, https://doi.org/10.5194/cp-13-573-
2017, 2017.

Jørgensen, B. B., Erez, J., Revsbech, P., and Cohen, Y.:
Symbiotic photosynthesis in a planktonic foraminiferan,
Globigerinoides sacculifer (Brady), studied with mi-
croelectrodes, Limnol. Oceanogr., 30, 1253–1267,
https://doi.org/10.4319/lo.1985.30.6.1253, 1985.

Keeling, C. D.: The Suess effect: ^{13}Carbon-^{14}Carbon interrela-
tions, Environ. Int., 2, 229–300, https://doi.org/10.1016/0160-
4120(79)90005-9, 1979.

Khatiwala, S., Schmittner, A., and Muglia, J.: Air-sea
disequilibrium enhances ocean carbon storage dur-
ing glacial periods, Science Advances, 5, eaaw4981,
https://doi.org/10.1126/sciadv.aaw4981, 2019.

Kimoto, K.: Planktic Foraminifera, 129–178, Springer Japan,
Tokyo, https://doi.org/10.1007/978-4-431-55130-0_7, 2015.

Köhler, P.: Anthropogenic CO$_2$ of high emission scenario compen-
sated after 3500 years of ocean alkalinization with an annually
constant dissolution of 5 Pg of olivine, Frontiers in Climate, 2,
575744, https://doi.org/10.3389/fclim.2020.575744, 2020.

Köhler, P.: Plio-Pleistocene simulations from a global
carbon cycle box model, PANGAEA [data set],
https://doi.org/10.1594/PANGAEA.940169, 2022.

Köhler, P. and Fischer, H.: Simulating changes in the ter-
restrial biosphere during the last glacial / interglacial
transition, Global Planet. Change, 43, 33–55,
https://doi.org/10.1016/j.gloplacha.2004.02.005, 2004.

Köhler, P. and Mulitza, S.: Mono-specific non-polar stacks
of δ^{13}C and δ^{18}O from the planktic foraminifera *G. ru-
ber* and *T. sacculifer* and simulation results of the ^{13}C
cycle across the last glacial cycle, PANGAEA [data set],
https://doi.org/10.1594/PANGAEA.963761, 2023.

Köhler, P. and Munhoven, G.: Late Pleistocene carbon cy-
cle revisited by considering solid Earth processes, Pa-

leoceanography and Paleoclimatology, 35, e2020PA004020, https://doi.org/10.1029/2020PA004020, 2020.

Köhler, P., Fischer, H., Munhoven, G., and Zeebe, R. E.: Quantitative interpretation of atmospheric carbon records over the last glacial termination, Global Biogeochem. Cy., 19, GB4020, https://doi.org/10.1029/2004GB002345, 2005.

Köhler, P., Fischer, H., and Schmitt, J.: Atmospheric $\delta^{13}CO_2$ and its relation to pCO_2 and deep ocean $\delta^{13}C$ during the late Pleistocene, Paleoceanography, 25, PA1213, https://doi.org/10.1029/2008PA001703, 2010.

Köhler, P., Nehrbass-Ahles, C., Schmitt, J., Stocker, T. F., and Fischer, H.: A 156 kyr smoothed history of the atmospheric greenhouse gases CO_2, CH_4, and N_2O and their radiative forcing, Earth Syst. Sci. Data, 9, 363–387, https://doi.org/10.5194/essd-9-363-2017, 2017a.

Köhler, P., Nehrbass-Ahles, C., Schmitt, J., Stocker, T. F., and Fischer, H.: Compilations and splined-smoothed calculations of continuous records of the atmospheric greenhouse gases CO_2, CH_4, and N_2O and their radiative forcing since the penultimate glacial maximum, PANGAEA [data set], https://doi.org/10.1594/PANGAEA.871273, 2017b.

Köhler, P., Adolphi, F., Butzin, M., and Muscheler, R.: Toward reconciling radiocarbon production rates with carbon cycle changes of the last 55,000 years, Paleoceanography and Paleoclimatology, 37, e2021PA004314, https://doi.org/10.1029/2021PA004314, 2022.

Langner, M. and Mulitza, S.: Technical note: PaleoDataView – a software toolbox for the collection, homogenization and visualization of marine proxy data, Clim. Past, 15, 2067–2072, https://doi.org/10.5194/cp-15-2067-2019, 2019.

Laskar, J., Robutel, P., Joutel, F., Gastineau, M., Correia, A. C. M., and Levrard, B.: A long term numerical solution for the insolation quantities of the Earth, Astron. Astrophys., 428, 261–285, https://doi.org/10.1051/0004-6361:20041335, 2004.

Linsley, B. K., Dunbar, R. B., Dassié, E. P., Tangri, N., Wu, H. C., Brenner, L. D., and Wellington, G. M.: Coral carbon isotope sensitivity to growth rate and water depth with paleo-sea level implications, Nat. Commun., 10, 2056, https://doi.org/10.1038/s41467-019-10054-x, 2019.

Lisiecki, L. E.: Atlantic overturning responses to obliquity and precession over the last 3 Myr, Paleoceanography, 29, 71–86, https://doi.org/10.1002/2013PA002505, 2014.

Lisiecki, L. E. and Raymo, M. E.: A Pliocene-Pleistocene stack of 57 globally distributed benthic $\delta^{18}O$ records, Paleoceanography, 20, PA1003, https://doi.org/10.1029/2004PA001071, 2005.

Lisiecki, L. E. and Stern, J. V.: Regional and global benthic $\delta^{18}O$ stacks for the last glacial cycle, Paleoceanography, 31, 1368–1394, https://doi.org/10.1002/2016PA003002, 2016.

Liu, Q., Kandasamy, S., Zhai, W., Wang, H., Veeran, Y., Gao, A., and Chen, C.-T. A.: Temperature is a better predictor of stable carbon isotopic compositions in marine particulates than dissolved CO_2 concentration, Commun. Earth Environ., 3, 303, https://doi.org/10.1038/s43247-022-00627-y, 2022.

Lloyd, J. and Farquhar, G. D.: ^{13}C discrimination during CO_2 assimilation by the terrestrial biosphere, Oecologia, 99, 201–215, 1994.

Lorrain, A., Pethybridge, H., Cassar, N., Receveur, A., Allain, V., Bodin, N., Bopp, L., Choy, C. A., Duffy, L., Fry, B., Goñi, N., Graham, B. S., Hobday, A. J., Logan, J. M., Mé-

nard, F., Menkes, C. E., Olson, R. J., Pagendam, D. E., Point, D., Revill, A. T., Somes, C. J., and Young, J. W.: Trends in tuna carbon isotopes suggest global changes in pelagic phytoplankton communities, Glob. Change Biol., 26, 458–470, https://doi.org/10.1111/gcb.14858, 2020.

Lund, D., Hertzberg, J., and Lacerra, M.: Carbon isotope minima in the South Atlantic during the last deglaciation: evaluating the influence of air-sea gas exchange, Environ. Res. Lett., 14, 055004, https://doi.org/10.1088/1748-9326/ab126f, 2019.

Lynch-Stieglitz, J., Valley, S. G., and Schmidt, M. W.: Temperature-dependent ocean-atmosphere equilibration of carbon isotopes in surface and intermediate waters over the deglaciation, Earth Planet. Sc. Lett., 506, 466–475, https://doi.org/10.1016/j.epsl.2018.11.024, 2019.

Ma, W., Tian, J., Li, Q., and Wang, P.: Simulation of long eccentricity (400-kyr) cycle in ocean carbon reservoir during Miocene Climate Optimum: Weathering and nutrient response to orbital change, Geophys. Res. Lett., 38, L10701, https://doi.org/10.1029/2011GL047680, 2011.

Marchal, O., Stocker, T. F., and Joos, F.: A latitude-depth, circulation-biogeochemical ocean model for paleoclimate studies. Development and sensitivities, Tellus B, 50, 290–316, https://doi.org/10.3402/tellusb.v50i3.16130, 1998.

Meinecke, G.: Isotopes (G. sacculifer) of sediment core GeoB1112-4, PANGAEA [data set], https://doi.org/10.1594/PANGAEA.54765, 1999.

Menking, J., Shackleton, S., Barker, S., Bauska, T., Brook, E., Buffen, A., Dyonisius, M., Petrenko, V., and Severinghaus, J.: Taylor Glacier CO_2 Isotope Data 74–59 kyr, U.S. Antarctic Program (USAP) Data Center [data set], https://doi.org/10.15784/601600, 2022a.

Menking, J. A., Shackleton, S. A., Bauska, T. K., Buffen, A. M., Brook, E. J., Barker, S., Severinghaus, J. P., Dyonisius, M. N., and Petrenko, V. V.: Multiple carbon cycle mechanisms associated with the glaciation of Marine Isotope Stage 4, Nat. Commun., 13, 5443, https://doi.org/10.1038/s41467-022-33166-3, 2022b.

Menviel, L., Joos, F., and Ritz, S.: Simulating atmospheric CO_2, ^{13}C and the marine carbon cycle during the Last Glacial-Interglacial cycle: possible role for a deepening of the mean remineralization depth and an increase in the oceanic nutrient inventory, Quaternary Sci. Rev., 56, 46–68, https://doi.org/10.1016/j.quascirev.2012.09.012, 2012.

Menviel, L., Mouchet, A., Meissner, K. J., Joos, F., and England, M. H.: Impact of oceanic circulation changes on atmospheric $\delta^{13}CO_2$, Global Biogeochem. Cy., 29, 1944–1961, https://doi.org/10.1002/2015GB005207, 2015.

Mojica Prieto, F. J. and Millero, F. J.: The values of $pK_1 + pK_2$ for the dissolution of carbonic acid in seawater, Geochim. Cosmochim. Ac., 66, 2529–2540, https://doi.org/10.1016/S0016-7037(02)00855-4, 2002.

Mulitza, S., Bickert, T., Bostock, H. C., Chiessi, C. M., Donner, B., Govin, A., Harada, N., Huang, E., Johnstone, H. J. H., Kuhnert, H., Langner, M., Lamy, F., Lembke-Jene, L., Lisiecki, L. E., Lynch-Stieglitz, J., Max, L., Mohtadi, M., Mollenhauer, G., Muglia, J., Nürnberg, D., Paul, A., Rühlemann, C., Repschläger, J., Saraswat, R., Schmittner, A., Sikes, E. L., Spielhagen, R. F., and Tiedemann, R.: World Atlas of late Quaternary Foraminiferal Oxygen and Carbon Isotope Ra-

tios (WA_Foraminiferal_Isotopes_2022), PANGAEA [data set], https://doi.org/10.1594/PANGAEA.936747, 2021.

Mulitza, S., Bickert, T., Bostock, H. C., Chiessi, C. M., Donner, B., Govin, A., Harada, N., Huang, E., Johnstone, H., Kuhnert, H., Langner, M., Lamy, F., Lembke-Jene, L., Lisiecki, L., Lynch-Stieglitz, J., Max, L., Mohtadi, M., Mollenhauer, G., Muglia, J., Nürnberg, D., Paul, A., Rühlemann, C., Repschläger, J., Saraswat, R., Schmittner, A., Sikes, E. L., Spielhagen, R. F., and Tiedemann, R.: World Atlas of late Quaternary Foraminiferal Oxygen and Carbon Isotope Ratios, Earth Syst. Sci. Data, 14, 2553–2611, https://doi.org/10.5194/essd-14-2553-2022, 2022.

Munhoven, G.: Modelling glacial-interglacial atmospheric CO_2 variations: the role of continental weathering, PhD thesis, Université de Liège, Liège, Belgium, http://hdl.handle.net/2268/161314 (last access: 16 November 2023), 1997.

Munhoven, G. and François, L. M.: Glacial-interglacial variability of atmospheric CO_2 due to changing continental silicate rock weathering: a model study, J. Geophys. Res., 101, 21423–21437, https://doi.org/10.1029/96JD01842, 1996.

Nederbragt, A. J.: The Effect of Seawater Carbonate Chemistry on the Stable Isotope Composition of Cibicidoides wuellerstorfi and Other Cibicidoides Species, Paleoceanography and Paleoclimatology, 38, e2023PA004667, https://doi.org/10.1029/2023PA004667, 2023.

Oliver, K. I. C., Hoogakker, B. A. A., Crowhurst, S., Henderson, G. M., Rickaby, R. E. M., Edwards, N. R., and Elderfield, H.: A synthesis of marine sediment core $\delta^{13}C$ data over the last 150 000 years, Clim. Past, 6, 645–673, https://doi.org/10.5194/cp-6-645-2010, 2010.

Oppo, D. W. and Fairbanks, R. G.: Carbon isotope composition of tropcial surface water during the past 22,000 years, Paleoceanography, 4, 333–351, https://doi.org/10.1029/PA004i004p00333, 1989.

Paillard, D.: The Plio-Pleistocene climatic evolution as a consequence of orbital forcing on the carbon cycle, Clim. Past, 13, 1259–1267, https://doi.org/10.5194/cp-13-1259-2017, 2017.

Pälike, H., Norris, R. D., Herrle, J. O., Wilson, P. A., Coxall, H. K., Lear, C. H., Shackleton, N. J., k. Tripati, A., and Wade, B. S.: The heartbeat of the Oligocene climate system, Science, 314, 1894–1898, https://doi.org/10.1126/science.1133822, 2006.

Peterson, C. D. and Lisiecki, L. E.: Deglacial carbon cycle changes observed in a compilation of 127 benthic $\delta^{13}C$ time series (20–6 ka), Clim. Past, 14, 1229–1252, https://doi.org/10.5194/cp-14-1229-2018, 2018.

Peterson, C. D., Lisiecki, L. E., and Stern, J. V.: Deglacial whole-ocean $\delta^{13}C$ change estimated from 480 benthic foraminiferal records, Paleoceanography, 29, 549–563, https://doi.org/10.1002/2013PA002552, 2014.

Pinho, T., Chiessi, C. M., Campos, M. C., Portilho-Ramos, R. C., Martínez-Méndez, G., Venancio, I. M., Nascimento, R. A., Crivellari, S., Albuquerque, A. L., Arz, H. W., Tiedemann, R., Bahr, A., and Mulitza, S.: Thermodynamic air-sea equilibration controls carbon isotopic composition of the South Atlantic thermocline during the last glacial period, Global Planet. Change, 229, 104223, https://doi.org/10.1016/j.gloplacha.2023.104223, 2023.

Pöppelmeier, F., Baggenstos, D., Grimmer, M., Liu, Z., Schmitt, J., Fischer, H., and Stocker, T. F.: The Effect of Past Saturation Changes on Noble Gas Reconstructions of Mean

Ocean Temperature, Geophys. Res. Lett., 50, e2022GL102055, https://doi.org/10.1029/2022GL102055, 2023.

R Core Team: R: A Language and Environment for Statistical Computing, R Foundation for Statistical Computing, Vienna, Austria, https://www.R-project.org (last access: 16 November 2023), 2023.

Reimer, P. J., Austin, W. E. N., Bard, E., Bayliss, A., Blackwell, P. G., Bronk Ramsey, C., Butzin, M., Cheng, H., Edwards, R. L., Friedrich, M., Grootes, P. M., Guilderson, T. P., Hajdas, I., Heaton, T. J., Hogg, A. G., Hughen, K. A., Kromer, B., Manning, S. W., Muscheler, R., Palmer, J. G., Pearson, C., van der Plicht, H., Reimer, R. W., Richards, D. A., Scott, E. M., Southon, J. R., Turney, C. S. M., Wacker, L., Adophi, F., Büntgen, U., Capano, M., Fahrni, S., Fogtmann-Schulz, A., Friedrich, R., Köhler, P., Kudsk, S., Miyake, F., Olsen, J., Reinig, F., Sakamoto, M., Sookdeo, A., and Talamo, S.: The IntCal20 Northern Hemisphere radiocarbon age calibration curve (0–55 cal kBP), Radiocarbon, 62, 725–757, https://doi.org/10.1017/RDC.2020.41, 2020.

Rohde, R. A. and Hausfather, Z.: The Berkeley Earth Land/Ocean Temperature Record, Earth Syst. Sci. Data, 12, 3469–3479, https://doi.org/10.5194/essd-12-3469-2020, 2020.

Romahn, S.: Western Indian Ocean circulation and climate variability on different time scales: a study based on stable oxygen and carbon isotopes, benthic foraminiferal assemblages and Mg/Ca paleothermometry, PhD thesis, Fachbereich Geowissenschaften, Universität Bremen, 95 pp., http://nbn-resolving.de/urn:nbn:de:gbv:46-00104138-17 (last access: 16 November 2023), 2014.

Roth, R. and Joos, F.: Model limits on the role of volcanic carbon emissions in regulating glacial-interglacial CO_2 variations, Earth Planet. Sc. Lett., 329–330, 141–149, https://doi.org/10.1016/j.epsl.2012.02.019, 2012.

Rubino, M., Etheridge, D. M., Trudinger, C. M., Allison, C. E., Battle, M. O., Langenfelds, R. L., Steele, L. P., Curran, M., Bender, M., White, J. W. C., Jenk, T. M., Blunier, T., and Francey, R. J.: A revised 1000-year atmospheric $\delta^{13}C$-CO_2 record from Law Dome and South Pole, Antarctica, J. Geophys. Res.-Atmos., 118, 8482–8499, https://doi.org/10.1002/jgrd.50668, 2013.

Russon, T., Paillard, D., and Elliot, M.: Potential origins of 400–500 kyr periodicities in the ocean carbon cycle: A box model approach, Global Biogeochem. Cy., 24, GB2013, https://doi.org/10.1029/2009GB003586, 2010.

Schmitt, J., Schneider, R., Elsig, J., Leuenberger, D., Lourantou, A., Chappellaz, J., Köhler, P., Joos, F., Stocker, T. F., Leuenberger, M., and Fischer, H.: Carbon isotope constraints on the deglacial CO_2 rise from ice cores, Science, 336, 711–714, https://doi.org/10.1126/science.1217161, 2012.

Schmittner, A., Gruber, N., Mix, A. C., Key, R. M., Tagliabue, A., and Westberry, T. K.: Biology and air–sea gas exchange controls on the distribution of carbon isotope ratios ($\delta^{13}C$) in the ocean, Biogeosciences, 10, 5793–5816, https://doi.org/10.5194/bg-10-5793-2013, 2013.

Schmittner, A., Bostock, H. C., Cartapanis, O., Curry, W. B., Filipsson, H. L., Galbraith, E. D., Gottschalk, J., Herguera, J. C., Hoogakker, B., Jaccard, S. L., Lisiecki, L. E., Lund, D. C., Martínez-Méndez, G., Lynch-Stieglitz, J., Mackensen, A., Michel, E., Mix, A. C., Oppo, D. W., Peterson, C. D., Repschläger, J., Sikes, E. L., Spero, H. J., and Waelbroeck, C.: Calibration of the carbon isotope composition

(δ^{13}C) of benthic foraminifera, Paleoceanography, 32, 512–530, https://doi.org/10.1002/2016PA003072, 2017.

Schneider, R., Schmitt, J., Köhler, P., Joos, F., and Fischer, H.: A reconstruction of atmospheric carbon dioxide and its stable carbon isotopic composition from the penultimate glacial maximum to the last glacial inception, Clim. Past, 9, 2507–2523, https://doi.org/10.5194/cp-9-2507-2013, 2013.

Shackleton, S., Seltzer, A., Baggenstos, D., and Lisiecki, L. E.: Benthic δ^{18}O records Earth's energy imbalance, Nat. Geosci., 16, 797–802, https://doi.org/10.1038/s41561-023-01250-y, 2023.

Shao, J., Stott, L. D., Menviel, L., Ridgwell, A., Ödalen, M., and Mohtadi, M.: The atmospheric bridge communicated the δ^{13}C decline during the last deglaciation to the global upper ocean, Clim. Past, 17, 1507–1521, https://doi.org/10.5194/cp-17-1507-2021, 2021.

Slowey, N. C.: The modern and glacial thermoclines along the Bahama Banks, PhD thesis, Massachusetts Institute of Technology and Woods Hole Oceanographic Institution, http://hdl.handle.net/1721.1/57634 (last access: 16 November 2023), 1990.

Smith, H. J., Fischer, H., Wahlen, M., Mastroianni, D., and Deck, B.: Dual modes of the carbon cycle since the Last Glacial Maximum, Nature, 400, 248–250, 1999.

Spero, H. J.: Do planktic foraminifera accurately record shifts in the carbon isotopic composition of seawater ΣCO_2?, Mar. Micropaleontol., 19, 275–285, https://doi.org/10.1016/0377-8398(92)90033-G, 1992.

Spero, H. J. and Lea, D. W.: Intraspecific stable isotope variability in the planktic foraminifera *Globigerinoides sacculifer*: Results from laboratory experiments, Mar. Micropaleontol., 22, 221–234, https://doi.org/10.1016/0377-8398(93)90045-Y, 1993.

Spero, H. J. and Williams, D. F.: Extracting environmental information from planktonic foraminiferal δ^{13}C data, Nature, 335, 717–719, https://doi.org/10.1038/335717a0, 1988.

Spero, H. J. and Williams, D. F.: Opening the carbon isotope "vital effect" black box 1. Seasonal temperatures in the euphotic zone, Paleoceanography, 4, 593–601, https://doi.org/10.1029/PA004i006p00593, 1989.

Spero, H. J., Lerche, I., and Williams, D. F.: Opening the carbon isotope "vital effect" black box, 2, Quantitative model for interpreting foraminiferal carbon isotope data, Paleoceanography, 6, 639–655, https://doi.org/10.1029/91PA02022, 1991.

Spero, H. J., Bijma, J., Lea, D. W., and Bemis, B. E.: Effect of seawater carbonate concentration on foraminiferal carbon and oxygen isotopes, Nature, 390, 497–500, https://doi.org/10.1038/37333, 1997.

Spero, H. J., Bijma, J., Lea, D. W., and Russell, A. D.: Deconvolving Glacial Ocean Carbonate Chemistry from the Planktonic Foraminifera Carbon Isotope Record, in: Reconstructing Ocean History: A Window into the Future, edited by Abrantes, F. and Mix, A. C., Springer US, Boston, MA, 329–342, https://doi.org/10.1007/978-1-4615-4197-4_19, 1999.

The MathWorks Inc.: MATLAB Version: 9.14.0.2206163 (R2023a), Natick, Massachusetts, United States, https://www.mathworks.com (last access: 16 November 2023), 2023.

Tierney, J. E., Zhu, J., King, J., Malevich, S. B., Hakim, G. J., and Poulsen, C. J.: Glacial cooling and climate sensitivity revisited, Nature, 584, 569–573, https://doi.org/10.1038/s41586-020-2617-x, 2020.

Verwega, M.-T., Somes, C. J., Schartau, M., Tuerena, R. E., Lorrain, A., Oschlies, A., and Slawig, T.: Description of a global marine particulate organic carbon-13 isotope data set, Earth Syst. Sci. Data, 13, 4861–4880, https://doi.org/10.5194/essd-13-4861-2021, 2021.

Vogel, J. C.: Variability of carbon isotope fractionation during photosynthesis, in: Stable isotopes and plant carbon–water relations, edited by Ehleringer, J. R., Hall, A. E., and Farquhar, G. D., Academic Press, San Diego, USA, 29–46, https://doi.org/10.1016/B978-0-08-091801-3.50010-6, 1993.

Wang, P., Li, Q., Tian, J., Jian, Z., Liu, C., Li, L., and Ma, W.: Long-term cycles in the carbon reservoir of the Quaternary ocean: a perspective from the South China Sea, Nat. Sci. Rev., 1, 119–143, https://doi.org/10.1093/nsr/nwt028, 2014.

Wirtz, K., Smith, S. L., Mathis, M., and Taucher, J.: Vertically migrating phytoplankton fuel high oceanic primary production, Nat. Clim. Change, 12, 750–756, https://doi.org/10.1038/s41558-022-01430-5, 2022.

Wolf-Gladrow, D. A., Bijma, J., and Zeebe, R. E.: Model simulation of the carbonate chemistry in the microenvironment of symbiont bearing foraminifera, Mar. Chem., 64, 181–198, https://doi.org/10.1016/S0304-4203(98)00074-7, 1999.

Young, J. N., Bruggeman, J., Rickaby, R. E. M., Erez, J., and Conte, M.: Evidence for changes in carbon isotopic fractionation by phytoplankton between 1960 and 2010, Global Biogeochem. Cy., 27, 505–515, https://doi.org/10.1002/gbc.20045, 2013.

Yun, K.-S., Timmermann, A., Lee, S.-S., Willeit, M., Ganopolski, A., and Jadhav, J.: A transient coupled general circulation model (CGCM) simulation of the past 3 million years, Clim. Past, 19, 1951–1974, https://doi.org/10.5194/cp-19-1951-2023, 2023.

Zahn-Knoll, R.: Spätquatäre Entwicklung von Küstenauftrieb und Tiefenwasserzirkulation im Nordost-Atlantik. Rekonstruktion anhand stabiler Isotope kalkschaliger Foraminiferen, PhD thesis, Christian-Albrechts-Universität zu Kiel, 111 pp., https://oceanrep.geomar.de/id/eprint/40044/ (last access: 16 November 2023), 1986.

Zeebe, R. E.: An explanation of the effect of seawater carbonate concentration on foraminiferal oxygen isotopes, Geochim. Cosmochim. Ac., 63, 2001–2007, https://doi.org/10.1016/S0016-7037(99)00091-5, 1999.

Zeebe, R. E. and Wolf-Gladrow, D. A.: CO_2 in Seawater: Equilibrium, Kinetics, Isotopes, vol. 65 of Elsevier Oceanography Book Series, Elsevier Science Publishing, Amsterdam, The Netherlands, 2001.

Zeebe, R. E., Bijma, J., and Wolf-Gladrow, D. A.: A diffusion-reaction model of carbon isotope fractionation in foraminifera, Mar. Chem., 64, 199–227, https://doi.org/10.1016/S0304-4203(98)00075-9, 1999.

Zeebe, R. E., Bijma, J., Hönisch, B., Sanyal, A., Spero, H. J., and Wolf-Gladrow, D. A.: Vital effects and beyond: a modelling perspective on developing palaeoceanographical proxy relationships in foraminifera, in: Biogeochemical Controls on Palaeoceanographic Environmental Proxies, Geological Society of London, https://doi.org/10.1144/SP303.4, 2008.

Zhang, J., Quay, P. D., and Wilbur, D. O.: Carbon isotope fractionation during gas-water exchange and dissolution of CO_2, Geochim. Cosmochim. Ac., 59, 107–114, 1995.

Zheng, B., Lucas, A. J., Franks, P. J. S., Schlosser, T. L., Anderson, C. R., Send, U., Davis, K., Barton, A. D., and

Sosik, H. M.: Dinoflagellate vertical migration fuels an intense red tide, P. Natl. Acad. Sci. USA, 120, e2304590120, https://doi.org/10.1073/pnas.2304590120, 2023.

Ziveri, P., Stoll, H., Probert, I., Klaas, C., Geisen, M., Ganssen, G., and Young, J.: Stable isotope "vital effects" in coccolith calcite, Earth Planet. Sc. Lett., 210, 137–149, https://doi.org/10.1016/S0012-821X(03)00101-8, 2003.